IEEE Access
Multidisciplinary ⋮ Rapid Review ⋮ Open Access Journal

Received May 21, 2019, accepted June 18, 2019, date of publication July 8, 2019, date of current version August 27, 2019.

Digital Object Identifier 10.1109/ACCESS.2019.2927326

Efficient Multidimensional Wideband Parameter Estimation for OFDM Based Joint Radar and Communication Systems

IVAN PODKURKOV[1], (Student Member, IEEE), JIANSHU ZHANG[2], (Member, IEEE), ADEL FIRADOVICH NADEEV[1], AND MARTIN HAARDT[2], (Fellow, IEEE)

[1]Department of Radioelectronic and Telecommunications Systems, Kazan National Research Technical University named after A. N. Tupolev, 420111 Kazan, Russia
[2]Communications Research Laboratory, Technische Universität Ilmenau, 98684 Ilmenau, Germany

Corresponding author: Ivan Podkurkov (podkiva@mail.ru)

This work was supported in part by the German Research Foundation (DFG), and in part by the Open Access Publication Fund of the TU Ilmenau.

ABSTRACT In this paper, we propose a new pre-processing technique for efficient multidimensional wideband parameter estimation. One application is provided by an orthogonal frequency division multiplexing-(OFDM) based joint radar and communication system, which uses SIMO architecture. In this paper, the estimated parameters are given by the range (time delay), the relative velocity, and the direction of arrival (DoA) pairs of the dominant radar targets. Due to the wideband assumption, the received signals on different subcarriers are incoherent and, therefore, cannot fully exploit the frequency diversity of the OFDM waveform. To estimate the parameters jointly and coherently on different subcarriers, we propose an interpolation-based coherent multidimensional parameter estimation framework, where the wideband measurements are transformed into an equivalent narrowband system. Then, narrowband multidimensional parameter estimation algorithms can be applied. In particular, a wideband R-D periodogram is introduced as a benchmark algorithm, and we develop the R-D Wideband Unitary Tensor-ESPRIT algorithm. The simulations show that the proposed coherent parameter estimation method significantly outperforms the direct application of narrowband parameter estimation algorithms to the wideband measurements. If the fractional bandwidth is significant and the SNR is not too low, the estimates provided by the narrowband estimation algorithms can become inconsistent. Moreover, the interpolation order should be chosen according to the SNR regime. In the low SNR regime, interpolation with a lower-order (i.e., linear interpolation) is recommended. For higher SNRs, we propose an interpolation with higher-order polynomials, e.g., fourth-order (cubic splines) or even higher.

INDEX TERMS ESPRIT, interpolation, joint radar and communication, periodogram, wideband OFDM.

I. INTRODUCTION

A joint radar and communication system can exploit the available physical resources such as spectrum and hardware components more efficiently compared to a traditional radar or communication system [2], [3]. To facilitate the equalization in a frequency selective environment, typically Orthogonal Frequency Division Multiplexing (OFDM) waveforms are used [4], [5]. The performance of a block transmission based joint radar and communication system was analyzed in [6], [7]. Automotive radar applications have attracted much attention, where the radar has become an important part of driver assistance and autonomous driving systems. Good overviews of such systems and algorithms can be found in [8] and [9].

A joint radar and communication system has been recently studied in [3] and [10] in an application to intelligent transportation systems (ITSs) [11], [12]. Both parts (namely, the communication part and the radar part) of such an integrated system can benefit from each other. For example, the locations of the radar targets can serve as a source of the channel state information (CSI) for the communication

The associate editor coordinating the review of this manuscript and approving it for publication was Xiaolong Chen.

part, or it can be used to estimate the relay geometry in systems with spatially random two-hop relaying [13]. In [3] the sub 6 GHz car-to-car OFDM communication standard IEEE 802.11p is used. The estimation of target distances and velocities has been studied and a one-dimensional periodogram-based algorithm has been proposed and analyzed. In [10] the joint radar and communication system uses the mmWave WLAN standard IEEE 802.11ad. A time domain correlation based parameter estimation method has been proposed. In both papers, a narrowband system model is considered and the proposed parameter estimation methods are search-based non-parametric methods. However, for critical scenes, high-resolution estimates are preferred because they can provide more accurate estimates. Moreover, since the range resolution of a radar is inversely proportional to the bandwidth, future joint radar and communication systems are likely to have a large bandwidth.

In the narrowband case, the estimation of the radar parameters, such as range, speed, and directions of arrival (DoAs) of the dominant radar targets in the joint radar and communication system can be interpreted as a multidimensional harmonic retrieval problem. But, since a joint radar and communication system is likely to use a large bandwidth, we consider the multidimensional wideband parameter estimation problem. There are several wideband extensions of narrowband DoA estimation algorithms [14]. In general, wideband parameter estimation algorithms can be divided into two classes [15], incoherent signal subspace processing and coherent signal subspace processing. In the former case, the parameter estimation is performed independently in different frequency bands using narrowband algorithms. Then the results are combined by averaging over the obtained estimates [16], [17]. The latter approach [18]–[21], [22], [23] uses a coherent combination of signal subspaces at different frequencies. Then the parameters are estimated using this enhanced combined signal subspace.

For coherent signal subspace processing, the aforementioned papers use a linear transformation of the data to focus the spatial steering vectors onto a reference frequency for some range of interest of harmonic frequencies. They exploit prior knowledge of the possible range of harmonic frequencies. A similar approach could also be used on the transmitter side to transform a fixed array geometry to another virtual array geometry with the required properties, e.g., to obtain a shift-invariance property required for ESPRIT-type algorithms [24].

Instead of using a least-squares fit to construct focusing matrices for a certain range of harmonic frequencies, one can consider transforming the received data as if it would be gathered by virtual arrays with frequency-dependent sensor positions to restore the narrowband manifold. This allows the coherent combination of data from different frequency bins. Any prior knowledge of the parameters of interest is not required. We refer to this approach as the interpolation based coherent approach because the transformation of the data is achieved by various interpolation techniques.

Although [15] served as a source of inspiration for our study, the core idea of the interpolation approach can be traced back to [25], [26]. A comparison of the interpolation approach to the approach with focusing matrices can be found in [27], where it has been shown that the latter in general has a degraded performance due to its intolerance to errors in preliminary angle estimates. The authors of [25] have used the FFT followed by zero-padding and the IFFT to interpolate the data, while [26] uses conventional resampling approaches in [28]. In [15], the authors apply the one-dimensional Shannon-Whittaker interpolation algorithm to a three-dimensional data set, followed by a 3-D canonical polyadic (CP) decomposition based parameter estimation method. The same method can also be extended to our problem. However, the CP decomposition has a significantly higher computational complexity compared to the HOSVD, which will be used in our application. Moreover, we decompose a real-valued tensor instead of a complex-valued tensor, which further reduces the computational complexity. It is worth stressing that the OFDM based joint radar and communication system concept proposed by [4] uses the prior knowledge of the transmitted signals, which allows obtaining the Vandermonde structure of the data in time and frequency. As a consequence, we can utilize it to extend DoA estimation algorithms to estimate range and Doppler parameters of the dominant radar targets.

In this paper, an interpolation based coherent parameter estimation framework is proposed to estimate the range (time delays), the relative velocities, and the angle of arrival (DoA) pairs of the dominant radar targets. We discuss several interpolation techniques that provide a balance between complexity, robustness, and interpolation errors. We consider piece-wise polynomial interpolation of different orders. We also compare them with Shannon-Whittaker interpolation that has been proposed in [1]. The linear and the cubic spline interpolation techniques have a residual error in the high SNR regime. To combat this effect, we also examine a higher-order (larger than four) spline interpolation techniques in this paper. Higher-order splines are able to provide smaller interpolation errors and improve the performance in the high SNR regime. But the higher-order splines are sensitive to noise distortions, e.g., in the low SNR regime, their performance is worse than that of the cubic spline interpolation. Therefore, we add an additional "denoising" step to our algorithm, aiming at reducing the influence of the noise when the higher-order splines are used. If the fractional bandwidth is significant and the SNR is not too low, the derived Wideband Unitary Tensor-ESPRIT algorithm provides a significant performance gain as compared to the direct application of narrowband multidimensional parameter estimation methods in such a wideband system.

Therefore, the contributions of this paper are summarized as follows:

- We consider a Joint Radar and Communication system based on OFDM, where the reflections of the transmitted signal are received by an antenna array and are used for multidimensional parameter estimation. In particular, we estimate the range, relative velocity and directions of arrival (DoA) of the dominant radar targets.

- The 4-D Wideband Unitary Tensor-ESPRIT (4-D Wideband-UTE) algorithm is proposed as an extension of the 4-D UTE with an interpolation based pre-processing technique for coherent multidimensional wideband parameter estimation.
- The simulation results show that a significant performance gain is achieved as compared to the direct application of narrowband algorithms to the wideband system, especially when the SNR is high or the fractional bandwidth is large.
- In particular, we propose to use linear interpolation for low SNRs or low fractional bandwidths, an interpolation based on cubic splines in case of high SNRs or high fractional bandwidths, and higher order splines in case of extremely high SNRs. For the latter scenario, we also develop an additional "denoising" step to enhance estimation accuracy.

The paper is organized as follows. In Section II we introduce the joint radar and communication system system concept and describe the system model. In Section III we propose a pre-processing technique that uses the interpolation approach to transform the data into an equivalent narrowband form. Then, in Section IV we derive wideband radar estimation algorithms, namely the 4-D periodogram and the 4-D Wideband Unitary Tensor-ESPRIT. Section V contains simulation results, and the conclusions are presented in Section VI.

A. NOTATION

Upper-case and lower-case bold-faced letters denote matrices and vectors, respectively. The expectation, conjugate, Hermitian transpose, and Moore-Penrose pseudo inverse are denoted by $\mathbb{E}\{\cdot\}$, $\{\cdot\}^*$, $\{\cdot\}^{\mathrm{H}}$, and $\{\cdot\}^+$, respectively. The $m \times m$ identity matrix is $\boldsymbol{I}_m$. Moreover, the $m \times m$ exchange matrix with ones on its antidiagonal and zeros elsewhere is $\boldsymbol{\Pi}_m$. An $m \times m$ left-$\boldsymbol{\Pi}$-real matrix $\boldsymbol{Q}_m$ satisfies $\boldsymbol{\Pi}_m \boldsymbol{Q}_m^* = \boldsymbol{Q}_m$. Furthermore, the absolute value is denoted by $|\cdot|$, the concatenation of matrices or tensors along the r-th dimension is denoted by $\sqcup_r$ $(r = 1, 2, 3, 4)$ [29], and the outer product between multi-linear vectors is $\circ$ [29]. The r-mode product between a tensor and a matrix is $\times_r$ [30]. The elements of vectors, matrices, and tensors are denoted as follows: $\boldsymbol{a}_{(i)}$ denotes i-th element of a vector $\boldsymbol{a}$, $\boldsymbol{A}_{(i,j)}$ denotes i, j-th element of a matrix $\boldsymbol{A}$, whereas for tensors $\mathcal{A}_{(i_1,i_2,\ldots,i_K)}$ denotes the respective element of a K-dimensional (K-D) tensor $\mathcal{A}$. Moreover, $\boldsymbol{B}_{(:,i)}$ and $\boldsymbol{B}_{(j,:)}$ denote the i-th column and the j-th row of a matrix $\boldsymbol{B}$. For a 4-dimensional tensor $\mathcal{C} \in \mathbb{C}^{I_1 \times I_2 \times I_3 \times I_4}$, the tensor $\mathcal{C}_{(:,:,i,:)} \in \mathbb{C}^{I_1 \times I_2 \times I_4}$ defines a subtensor that contains all elements with the 3-rd index fixed to i, stacked in proper order.

II. PRELIMINARY

In this section we introduce basic concepts of the joint radar and communication system in Subsection II-A and present its system model in Subsection II-B.

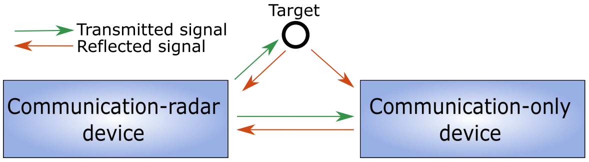

(a) Communication-radar device to communication-only device (forward-link)

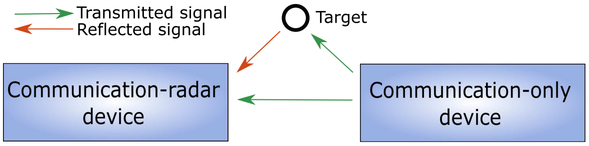

(b) Communication-only device to Communication-radar device (backward-link)

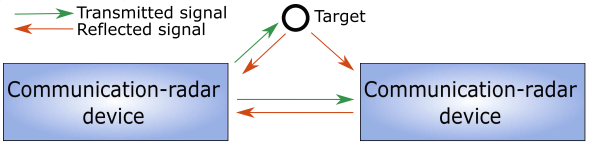

(c) Communication-radar to Communication-radar device (forward or backward link)

FIGURE 1. **Two-way communication concept.**

A. DESIGN CONCEPT OF THE JOINT RADAR AND COMMUNICATION SYSTEM

We consider an OFDM based joint radar and communication system with a co-located single transmit antenna and multiple receive antennas. The joint radar and communication system concept, proposed in [4] and described in detail in [3], assumes simultaneous functioning of both radar and communication systems. The same OFDM modulated signal is used for radar estimation and one-way communication. We assume that the radar and the communication system use the same RF components [3].

The two-way communication with the communication-radar device depends on whether it is communicating with a communication-only device (the one that can only transmit and receive OFDM signals), or another communication-radar device. Those possible cases are depicted in Figure 1. When a communication-radar device transmits to a communication-only device ("forward-link", Figure 1a), the radar receiver is turned on and is able to process the reflections from the radar targets. The communication-only device's receiver is also turned on and is able to receive and detect the signal transmitted from the communication-radar device. Thus, two functions (namely, radar and communication) are performed using the same frequency and time resources. The transmitter of the communication-only device is shut off during this period. The transmission from the communication-only device to the communication-radar device uses orthogonal time-frequency resources - either different subcarriers or different time slots - "backward-link", as depicted in Figure 1b. If two communication-radar devices are involved (Figure 1c), the two transmitters cannot transmit at the same time and on the same subcarriers. If the simultaneous functioning of both radars is needed, the radar system of the second device should use orthogonal time-frequency resources.

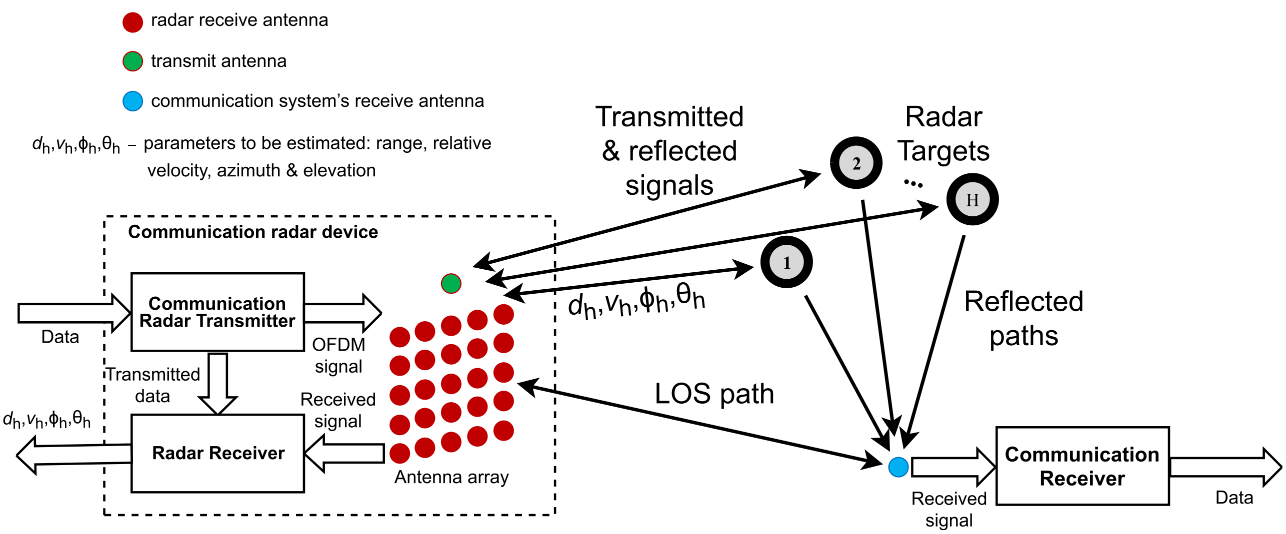

FIGURE 2. Joint radar and communication system design concept. The communication-radar device on the left is able to perform both communication with the communication receiver on the right and radar sensing of the radar targets in the middle at the same time using one transmitted OFDM signal.

It should be noted here that the considered system model is closely related to the two-hop relaying system with a random geometry described in [13]. If viewed from that perspective, the communication-radar device can transmit in the first stage of the relaying process. The results of the radar processing, namely the estimates of the locations of the relays (or dominant radar targets) can then be utilized as CSI to combat multipath effects in the communication system.

Therefore, for simplicity, we consider a one-way data flow as depicted in Figure 2. In this paper, we focus on the radar function, i.e., the estimation of the target parameters only, since the performance of both functions of the systems, namely communication and radar, is mainly coupled through the parametrization of the system. This issue has already been discussed in the literature, cf. [3], [4], [31], [32].

The communication-radar device transmits the OFDM data, intended for the communication and/or for the radar functions. When the radar functions are activated, the communication-radar device receives and processes the transmitted signal reflected from the radar targets. Those targets could be cars, road signs, or road fences, and also the communication partner itself in the context of automotive radar. In this example, the communication-radar device is equipped with a uniform rectangular array (URA) at the receiver (red dots in Figure 2), which is assumed to be co-located with the transmitter.

The considered joint radar and communication system uses the following steps:

1) The communication-radar device transmits the OFDM modulated communication signal using one transmit antenna (green dot in Figure 2).
2) The transmitted signal propagates towards the radar targets and the communication receiver.
3) The transmitted signal is reflected from the radar targets in all directions. It is also possible that the signal is reflected from the communication receiver itself (line of sight (LOS) path) if it has a high enough radar cross section (RCS).
4) The reflected signals propagate back towards the communication-radar device and also towards the communication receiver. The transmitted signal propagates via H dominant paths with range d_h and relative velocity v_h, where $h = 1, 2, \ldots, H$.
5) The reflected signals then impinge on the receive antenna array (red dots in Figure 2). Since it is assumed that the communication-radar device transmit antenna and the receive antenna array are co-located, the directions of departure (DoDs) and the directions of arrival (DoAs) are approximately equal. This reduces the problem to four dimensions and facilitates the estimation of azimuth and elevation angles of the targets.
6) The radar receiver processes the received reflected signals and estimates the parameters of H dominant radar targets. Obviously, the radar receiver knows the transmitted communication data. Therefore, it can eliminate the transmitted data from the received signal, as described in [3], [4].

We assume that the direct path interference is handled either in hardware (e.g., through shielding) or in software, or both [3]. Moreover, in case of a non-static scenario (relative velocities of radar targets are non-zero), the Doppler shifts from each of the targets introduce inter-carrier interference (ICI) for OFDM signal, which then prevents from ideal elimination of transmitted data from the received signal in (2). However, for the system parameters of interest, the effect of such distortions is not critical. Moreover, it can be shown that even when ICI is introduced into the model the performance

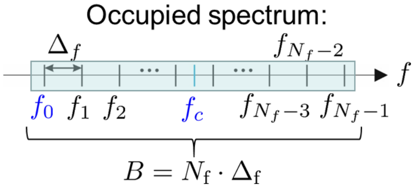

FIGURE 3. Spectrum, occupied by OFDM signal, where f_{n_f} denotes the frequency of the n_f-th subcarrier, and N_f is the total number of subcarriers. The Δ_f is the subcarrier spacing.

is improved by using the proposed wideband pre-processing. The received signal on each subcarrier, in that case, contains interference from all other subcarriers. Considering that that interference can be expressed explicitly in terms of parameters of interest (distances, relative velocities, and DoAs), an iterative estimation algorithm can be developed, which subtracts that interference from each subcarrier using the initial estimates of the parameters. Those, in turn, can be obtained either from a previous estimation run or by using element-wise division as as explained in Subsection II-B and running the whole estimation algorithm in order to get initial estimates.

B. SYSTEM MODEL

Let us assume that there is a uniform rectangular array of $M_x \times M_y$ antennas at the radar receiver. The h-th radar target ($h \in \{1, \cdots, H\}$) is parametrized by the time delay $\tau_h = \frac{2d_h}{c}$, where d_h denotes the distance between the radar and the h-th target, the relative velocity ν_h and the DoA pair (ϕ_h, θ_h), where ϕ_h and θ_h represent the azimuth angle and the elevation angle, respectively. We have $-\pi \leq \phi_h < \pi$, $0 \leq \theta_h < \pi/2$. The radar estimation is performed over an OFDM frame consisting of N_t OFDM symbols. Each OFDM symbol has N_f subcarriers and a FFT of length N_fft ($N_\mathrm{fft} \geq N_f$) is applied to transform it to the time domain. Hence we assume that the parameters of the scenario (target's range, relative velocities and DoAs) do not change over the N_t OFDM symbols. Let f_{n_f} denote the frequency on the n_f-th subcarrier ($n_f \in \{0, \cdots, N_f - 1\}$), which is defined as $f_{n_f} = f_0 + n_f \cdot \Delta_f$, where f_0 is the carrier frequency at the lower end of the band and Δ_f is the subcarrier spacing. Note that in a narrowband system we assume $f_{n_f} \approx f_0$, as depicted in Figure 3.

Then the received uniformly sampled discrete-time signal at the (m_x, m_y)-th antenna on the n_f-th subcarrier in the n_t-th OFDM symbol is written as

$$\begin{aligned} y_{m_x,m_y,n_f}[n_t] = \sum_{h=1}^{H} \tilde{k}_h e^{j\beta_h} \cdot \\ \cdot e^{-j2\pi\tau_h n_f \Delta_f} \cdot e^{j2\pi n_t \frac{f_{n_f} T_0}{c} \nu_h} \cdot e^{j2\pi m_x \frac{f_{n_f} \Delta_x}{c} u_h} \cdot \\ \cdot e^{j2\pi m_y \frac{f_{n_f} \Delta_y}{c} v_h} \cdot s_{n_f}[n_t] + z_{m_x,m_y,n_f}[n_t], \quad (1) \end{aligned}$$

where $m_x \in \{0, \cdots, M_x - 1\}$, $m_y \in \{0, \cdots, M_y - 1\}$, $n_t \in \{0, \cdots, N_t - 1\}$, $\tilde{k}_h = \sqrt{\frac{c^2 \sigma_{\mathrm{RCS},h}}{(4\pi)^3 d_h^4 f_c^2}}$ is the unknown attenuation coefficient defined as in [3], $\sigma_{\mathrm{RCS},h}$ denotes the radar cross-section factor, and c is the speed of the light. We assume that $\tilde{k}_h$ does not depend on the carrier index n_f. The OFDM symbol duration is given by $T_0 = \frac{1}{\Delta_f} + T_\mathrm{CP}$, where T_CP is the duration of the cyclic prefix. A random phase shift is denoted as β_h. The transmitted symbol is $s_{n_f}[n_t] \in \mathbb{C}$, and the transmit power is restricted such that $\mathrm{E}\{\sum_{n_f=1}^{N_\mathrm{fft}} |s_{n_f}[n_t]|^2\} = P_\mathrm{T}, \forall n_t$. The term $z_{m_x,m_y,n_f}[n_t]$ denotes the zero-mean noise with variance $\mathbb{E}\{|z_{m_x,m_y,n_f}[n_t]|^2\} = \sigma_\mathrm{n}^2, \forall m_x, m_y, n_f, n_t,$ uncorrelated along all measurement dimensions. Furthermore, we define the direction cosines $u_h = \cos(\phi_h)\cos(\theta_h)$ and $v_h = \sin(\phi_h)\cos(\theta_h)$, and the antenna spacings are denoted as Δ_x and Δ_y.

The communication signal $s_{n_f}[n_t]$ is known at the co-located radar receiver. Therefore, it can be removed from equation (1) by division and we obtain

$$\begin{aligned} &\check{r}_{m_x,m_y,n_f}[n_t] \\ &\quad = y_{m_x,m_y,n_f}[n_t]/s_{n_f}[n_t] \\ &\quad = \sum_{h=1}^{H} \tilde{k}_h e^{j\beta_h} \cdot e^{-j2\pi\tau_h n_f \Delta_f} \cdot e^{j2\pi n_t \frac{f_{n_f} T_0}{c} \nu_h} \\ &\qquad \cdot e^{j2\pi m_x \frac{f_{n_f} \Delta_x}{c} u_h} \cdot e^{j2\pi m_y \frac{f_{n_f} \Delta_y}{c} v_h} + \check{z}_{m_x,m_y,n_f}[n_t]. \quad (2) \end{aligned}$$

Note that the harmonic frequencies in (2) depend on the subcarrier index n_f. Therefore we refer to this model of measurements as the ''wideband'' model. If the noise $z_{m_x,m_y,n_f}[n_t]$ is also assumed to be zero mean circularly symmetric complex Gaussian (ZMCSCG), then the statistics of $\check{z}_{m_x,m_y,n_f}[n_t] = z_{m_x,m_y,n_f}[n_t]/s_{n_f}[n_t]$ remain unchanged if we assume that $s_{n_f}[n_t]$ are identically and independently distributed (i.i.d.) and generated from a constant modulus modulations, e.g., BPSK or QPSK [3].

It is then natural to stack measurements along all measurement dimensions - frequency, time, and space (x- and y-axes) into one measurement tensor $\check{\mathcal{R}}$ that is defined as

$$\check{\mathcal{R}} = \check{\mathcal{S}} + \check{\mathcal{Z}} \in \mathbb{C}^{M_x \times M_y \times N_f \times N_t}, \quad (3a)$$

where the tensors $\check{\mathcal{S}}$, $\check{\mathcal{Z}}$, and $\check{\mathcal{R}}$ are defined as

$$\begin{aligned} \check{\mathcal{S}}_{(m_x,m_y,n_f,n_t)} &= \sum_{h=1}^{H} \tilde{k}_h e^{j\beta_h} \cdot e^{-j2\pi\tau_h n_f \Delta_f} \\ &\quad \cdot e^{j2\pi n_t \frac{f_{n_f} T_0}{c} \nu_h} \cdot e^{j2\pi m_x \frac{f_{n_f} \Delta_x}{c} u_h} \cdot e^{j2\pi m_y \frac{f_{n_f} \Delta_y}{c} v_h}. \end{aligned} \quad (3b)$$

$$\check{\mathcal{Z}}_{(m_x,m_y,n_f,n_t)} = \check{z}_{m_x,m_y,n_f}[n_t] \quad (3c)$$

$$\check{\mathcal{R}}_{(m_x,m_y,n_f,n_t)} = \check{r}_{m_x,m_y,n_f}[n_t] \quad (3d)$$

Given $\check{\mathcal{R}}$, our goal is to coherently estimate the parameters τ_h, ν_h, ϕ_h, and θ_h for each $h \in \{1, \cdots, H\}$. Although the estimation can be provided simply by using just one subcarrier, this estimator would not fully exploit the frequency diversity of the OFDM waveform. Moreover, it will limit the range resolution of the radar, which depends on the bandwidth of the effective waveform. It is our goal to develop coherent multidimensional parameter estimation methods which use all the subcarriers jointly.

III. INTERPOLATION BASED COHERENT PARAMETER ESTIMATION

Our proposed interpolation based coherent parameter estimation concept consists of two steps. In the first step, the received signals on different subcarriers are preprocessed by using an interpolation algorithm described in Subsection III-A such that an equivalent narrowband OFDM system is obtained, i.e., that has the effective subcarrier frequency $\tilde{f}_{n_f} = f_0, \forall n_f$. Additionally, the "denoising" pre-processing described in Subsection III-B might be added to the first step to improve the estimation performance. In the second step, multidimensional parameter estimation schemes such as the low complexity R-D periodogram described in Subsection III-C or the high resolution R-D Unitary Tensor-ESPRIT algorithm described in Subsection III-D are applied to the equivalent narrowband OFDM signal.

A. PRE-PROCESSING VIA INTERPOLATION

The goal of the pre-processing step is to obtain an equivalent narrowband model of (2), i.e.,

$$\begin{aligned} r_{m_x,m_y,n_f}[n_t] &= \sum_{h=1}^{H} \tilde{k}_h e^{j\beta_h} e^{-j2\pi\tau_h n_f \Delta_f} \cdot e^{j2\pi n_t \frac{f_0 T_0}{c} v_h} \\ &\cdot e^{j2\pi m_x \frac{f_0 \Delta_x}{c} u_h} \cdot e^{j2\pi m_y \frac{f_0 \Delta_y}{c} v_h} + z_{m_x,m_y,n_f}[n_t], \end{aligned} \tag{4}$$

where $z_{m_x,m_y,n_f}[n_t]$ is zero-mean uncorrelated noise. As in (3), we construct a narrowband measurement tensor $\mathcal{R}$ that can be expressed in terms of signal tensor $\mathcal{S}$ and noise tensor $\mathcal{Z}$. The narrowband data model can be written as

$$\mathcal{R} = \underbrace{\sum_{h=1}^{H} k_h \cdot \boldsymbol{a}_h \circ \boldsymbol{b}_h \circ \boldsymbol{c}_h \circ \boldsymbol{d}_h}_{\mathcal{S}} + \mathcal{Z} \in \mathbb{C}^{M_x \times M_y \times N_f \times N_t}, \tag{5}$$

where $k_h = \tilde{k}_h e^{j\beta_h}$, $\mathcal{Z}_{(m_x,m_y,n_f,n_t)} = z_{m_x,m_y,n_f}[n_t]$, and we have

$$\begin{aligned} \boldsymbol{a}_h &= \left[1 \; e^{j2\pi \frac{f_0 \Delta_x}{c} u_h} \; \dots \; e^{j2\pi (M_x - 1) \frac{f_0 \Delta_x}{c} u_h}\right]^T \in \mathbb{C}^{M_x} \\ \boldsymbol{b}_h &= \left[1 \; e^{j2\pi \frac{f_0 \Delta_y}{c} v_h} \; \dots \; e^{j2\pi (M_y - 1) \frac{f_0 \Delta_y}{c} v_h}\right]^T \in \mathbb{C}^{M_y} \\ \boldsymbol{c}_h &= \left[1 \; e^{-j2\pi \tau_h \Delta_f} \; \dots \; e^{-j2\pi \tau_h (N_f - 1)\Delta_f}\right]^T \in \mathbb{C}^{N_f} \\ \boldsymbol{d}_h &= \left[1 \; e^{j2\pi \frac{f_0 \; T_0}{c} v_h} \; \dots \; e^{j2\pi (N_f - 1) \frac{f_0 \; T_0}{c} v_h}\right]^T \in \mathbb{C}^{N_t} \end{aligned}$$

The tensors $\mathcal{S}$, $\mathcal{R}$, and $\mathcal{Z}$ can be seen as 4-dimensional samples of continuous functions $s(x, y, f, t)$, $r(x, y, f, t)$, and $z(x, y, f, t)$ of four arguments - the spatial coordinates x and y, the frequency f, and the time t

$$\begin{aligned} s(x, y, f, t) &= \sum_{h=1}^{H} k_h e^{-j2\pi \tau_h f} \cdot e^{j2\pi \frac{f_0}{c} v_h t} \\ &\cdot e^{j2\pi \frac{f_0}{c} u_h x} \cdot e^{j2\pi \frac{f_0}{c} v_h y} \end{aligned} \tag{6a}$$

$$r(x, y, f, t) = s(x, y, f, t) + z(x, y, f, y) \tag{6b}$$

with the 4-dimensional "original" sampling grid

$$\begin{aligned} \mathcal{G}^o = \{(x, y, f, t) : x &= m_x \Delta_x, \quad y = m_y \Delta_y, \\ f &= f_{n_f}, \; t = n_t T_0\} \end{aligned} \tag{7}$$

where $z(x, y, f, t)$ is a realization of a zero-mean complex additive noise.

The wideband tensors $\breve{\mathcal{R}}$, $\breve{\mathcal{S}}$ and $\breve{\mathcal{Z}}$ can be expressed in the same fashion as

$$\begin{aligned} \breve{s}(x, y, f, t) &= \sum_{h=1}^{H} k_h \, e^{-j2\pi \tau_h f} \cdot e^{j2\pi \frac{f}{c} v_h t} \\ &\cdot e^{j2\pi \frac{f}{c} u_h x} \cdot e^{j2\pi \frac{f}{c} v_h y} \end{aligned} \tag{8a}$$

$$\breve{r}(x, y, f, t) = \breve{s}(x, y, f, t) + \breve{z}(x, y, f, y) \tag{8b}$$

having the same sampling grid as in (7), where $\breve{z}(x, y, f, t)$ is also another realization of a zero-mean complex additive noise.

The narrowband model assumes that the measurements are obtained by a discretization of (6b) using the sampling grid $\mathcal{G}^o$ defined in (7). The measurements, in this case, are modeled by (5). On the contrary, in the wideband model, the measurements are obtained by a discretization of (8b) using the same sampling grid $\mathcal{G}^o$. In this case, the measurements are modeled by (3).

The main idea of interpolation pre-processing is to compute an equivalent narrowband approximation of the wideband measurements in (2). Then, multidimensional narrowband high-resolution parameter estimation algorithms can be applied. To this end, we define a new sampling grid for the wideband model

$$\begin{aligned} \mathcal{G}^i = \{(x, y, f, t) : \; x &= m_x \frac{f_0}{f_{n_f}} \Delta_x, \; y = m_y \frac{f_0}{f_{n_f}} \Delta_y, \\ f &= f_{n_f}, \; t = n_t \frac{f_0}{f_{n_f}} T_0\} \end{aligned} \tag{9}$$

such that the sampling intervals become smaller as the frequency increases. Consequently, the ratios between harmonics frequencies and sampling frequencies (inverses ofsampling intervals Δ_x, Δ_y and T_0) stay constant along subcarriers and are equal to those in the narrowband model in (5).

It is evident that perfect sampling according to (9) is not possible due to practical limitations. Therefore, we resort to multidimensional interpolation techniques, which provide an approximation of (5) based on (3) using a mapping function g

$$\tilde{\mathcal{R}}^i = g(\breve{\mathcal{R}}) \approx \mathcal{R} \tag{10a}$$

$$g : \mathbb{C}^{M_x \times M_y \times N_f \times N_t} \rightarrow \mathbb{C}^{M_x \times M_y \times N_f \times N_t} \tag{10b}$$

To this end, we use different sampling intervals on each subcarrier n_f. For a given subcarrier index n_f, we can see from (9) that we have a 3-dimensional sampling rate conversion, where the sampling intervals have to be changed from Δ_x, Δ_y, and T_0 to $\frac{f_0}{f_{n_f}}\Delta_x$, $\frac{f_0}{f_{n_f}}\Delta_y$, and $\frac{f_0}{f_{n_f}}T_0$, respectively. We define the interpolation pre-processing step for subcarrier n_f as

$$\begin{aligned} \tilde{\mathcal{R}}^i_{n_f} &= g_{n_f}\left(\breve{\mathcal{R}}_{n_f}\right) \in \mathbb{C}^{M_x \times M_y \times N_t}, \\ \forall n_f &\in \{0, \ldots, N_f - 1\} \end{aligned} \tag{11}$$

where $\breve{\mathcal{R}}_{n_f} = \breve{\mathcal{R}}_{(:,:,n_f,:)}$ and $\tilde{\mathcal{R}}^i_{n_f} = \tilde{\mathcal{R}}^i_{(:,:,n_f,:)}$ are the subtensors of the measurements and the interpolated tensor obtained on the n_f-th subcarrier, respectively, and $g_{n_f}(\cdot)$ is an interpolating function for subcarrier n_f.

In this paper, we consider piece-wise polynomial interpolation techniques, that include linear interpolation (2-nd order spline), cubic spline interpolation with not-a-knot end conditions (4-th order spline), and also higher-order spline interpolation techniques [33]. If the spline interpolation technique uses polynomials of degree n, then it is referred to as an $(n+1)$-th order spline. For example, the cubic spline is a fourth order spline since it uses polynomials of degree 3 (the highest power of such polynomials is equal to n). Linear and cubic spline interpolation techniques are essentially linear in the data. In the 1-dimensional case, they can be expressed as a linear transformation of the data samples. The extension to 3-dimensional interpolation is a simple sequential application of 1-dimensional interpolation in each dimension, leading to a trilinear transformation of $\breve{\mathcal{R}}_{n_f}$. The interpolation preprocessing can be expressed as

$$g^L_{n_f}\left(\breve{\mathcal{R}}_{n_f}\right) = \breve{\mathcal{R}}_{n_f} \times_1 \boldsymbol{L}_{\Delta_{n_f},M_x} \times_2 \boldsymbol{L}_{\Delta_{n_f},M_y} \times_3 \boldsymbol{L}_{\Delta_{n_f},N_t} \tag{12a}$$

for the linear interpolation and

$$g^S_{n_f}\left(\breve{\mathcal{R}}_{n_f}\right) = \breve{\mathcal{R}}_{n_f} \times_1 \boldsymbol{S}_{\Delta_{n_f},M_x} \times_2 \boldsymbol{S}_{\Delta_{n_f},M_y} \times_3 \boldsymbol{S}_{\Delta_{n_f},N_t} \tag{12b}$$

for the cubic spline interpolation, where $\Delta_{n_f} = \frac{f_0}{f_{n_f}}$ is the sample rate conversion factor (equal for all measurement dimensions), $g^L_{n_f}$ and $g^S_{n_f}$ denote the linear and spline interpolation functions and $\boldsymbol{L}_{\Delta,N}, \boldsymbol{S}_{\Delta,N} \in \mathbb{R}^{N \times N}$ are the interpolation matrices, that depend on the conversion factor and the number of samples in the respective dimension. The detailed description of the applied interpolation techniques and the derivation of the $\boldsymbol{L}_{\Delta,N}$ and $\boldsymbol{S}_{\Delta,N}$ matrices are found in Appendices A and B.

It should be mentioned that under ideal conditions a perfect resampling is provided by the Shannon-Whittaker interpolation [34], which is also used in [15]. However, in practice, the Shannon-Whittaker interpolation cannot provide perfect reconstruction for a time-limited signal and it has high computational complexity. Therefore, this motivates us to study piece-wise polynomial interpolation methods that have a much lower computational cost. In Section IV, we also compare their performance to that of Shannon-Whittaker interpolation.

B. DENOISING VIA TRUNCATED HOSVD FOR EACH SUBCARRIER

The subtensors $\breve{\mathcal{R}}_{n_f}$, defined in (11), follow a noise corrupted low-rank model

$$\breve{\mathcal{R}}_{n_f} = \sum_{h=1}^{H} k_h e^{-j2\pi\tau_h n_f \Delta_f} \cdot \boldsymbol{a}^{n_f}_h \circ \boldsymbol{b}^{n_f}_h \circ \boldsymbol{d}^{n_f}_h + \breve{\mathcal{Z}}_{n_f}, \tag{13}$$

where

$$\begin{aligned} \boldsymbol{a}^{n_f}_h &= \left[1 \; e^{j2\pi\frac{f_{n_f}\Delta_x}{c}u_h} \; \ldots \; e^{j2\pi(M_x-1)\frac{f_{n_f}\Delta_x}{c}u_h}\right]^T \in \mathbb{C}^{M_x} \\ \boldsymbol{b}^{n_f}_h &= \left[1 \; e^{j2\pi\frac{f_{n_f}\Delta_y}{c}v_h} \; \ldots \; e^{j2\pi(M_y-1)\frac{f_{n_f}\Delta_y}{c}v_h}\right]^T \in \mathbb{C}^{M_y} \\ \boldsymbol{d}^{n_f}_h &= \left[1 \; e^{j2\pi\frac{f_{n_f}T_0}{c}\nu_h} \; \ldots \; e^{j2\pi(N_t-1)\frac{f_{n_f}T_0}{c}\nu_h}\right]^T \in \mathbb{C}^{N_t} \end{aligned}$$

This fact motivates us to consider one more additional preprocessing step for $\breve{\mathcal{R}}_{n_f}$, low-rank approximation using the truncated Higher Order SVD (HOSVD) for each $n_f \in \{0, \ldots, N_f - 1\}$. This step reduces the noise influence and is beneficial in some scenarios, where higher-order spline interpolation techniques are used. We further refer to it as the "denoising" step.

Define the HOSVD of $\breve{\mathcal{R}}_{n_f}$ as (following equation (18) of [29])

$$\breve{\mathcal{R}}_{n_f} = \mathcal{S} \times_1 \boldsymbol{U}^t_{n_f} \times_2 \boldsymbol{U}^x_{n_f} \times_3 \boldsymbol{U}^y_{n_f} \tag{14}$$

where $\boldsymbol{U}^t_{n_f} \in \mathbb{C}^{N_t \times N_t}$, $\boldsymbol{U}^x_{n_f} \in \mathbb{C}^{M_x \times M_x}$, $\boldsymbol{U}^y_{n_f} \in \mathbb{C}^{M_y \times M_y}$, and $\mathcal{S} \in \mathbb{C}^{N_t \times M_x \times M_y}$. Then, the truncated HOSVD of $\breve{\mathcal{R}}_{n_f}$ of order H is given as

$$\breve{\mathcal{R}}^d_{n_f} = \mathcal{S}^{[s]} \times_1 \boldsymbol{U}^{t,[s]}_{n_f} \times_2 \boldsymbol{U}^{x,[s]}_{n_f} \times_3 \boldsymbol{U}^{y,[s]}_{n_f} \tag{15}$$

where $p_t = \min(N_t, H), p_x = \min(M_x, H), p_y = \min(M_y, H)$, $\boldsymbol{U}^{t,[s]}_{n_f} \in \mathbb{C}^{N_t \times p_t}$, $\boldsymbol{U}^{x,[s]}_{n_f} \in \mathbb{C}^{M_x \times p_x}$, $\boldsymbol{U}^{y,[s]}_{n_f} \in \mathbb{C}^{M_y \times p_y}$, and $\mathcal{S} \in \mathbb{C}^{p_t \times p_x \times p_y}$. Note that in our application H is the number of targets that can be obtained by using an appropriate model order selection algorithm, as explained in [35]. In this paper H is assumed to be known.

The new tensor $\breve{\mathcal{R}}^d_{n_f}$ is then used instead of $\breve{\mathcal{R}}_{n_f}$ in (12a) or (12b).

C. 4-D PERIODOGRAM

After obtaining the equivalent narrowband signal model in (10a) we can use the multidimensional parameter estimation methods to estimate τ_h, ν_h, ϕ_h, and θ_h. The first algorithm we introduce is the 4-D periodogram as an extension of the 2-D periodogram described in [3]. A one-dimensional periodogram is the easiest way for spectral estimation, i.e., for a given sequence of N discrete samples $a(k)$ we compute [36]

$$S(f) = \frac{1}{N}\left|\sum_{k=0}^{N-1} a(k)e^{j2\pi fk}\right|^2.$$

Then the spectral components are obtained by searching the peaks in $S(f)$. Furthermore, a digital domain periodogram is realized using a T-length FFT of the discrete samples. Therefore the resolution is proportional to T. In our case, a four-dimensional periodogram is required of length p_1, p_2, p_3, and p_4, respectively. To this end we perform the FFTs over four dimensions sequentially. Let $\grave{\mathcal{R}} \in \mathbb{C}^{p_1 \times p_2 \times p_3 \times p_4}$ denote a tensor, whose r-th dimension ($r \in \{1, 2, 3, 4\}$) is obtained by truncating the slices along the r-th dimension of $\tilde{\mathcal{R}}^i$ if p_r is smaller than the length of the r-th dimension of $\tilde{\mathcal{R}}^i$, or by padding zero slices along the r-th dimension of $\tilde{\mathcal{R}}^i$ if p_r is not less than the length of the r-th dimension of $\tilde{\mathcal{R}}^i$. Let us also define the ratios between the original number of measurements to the dimensions of $\grave{\mathcal{R}}$ as $k_x = p_1/M_x$, $k_y = p_2/M_y$, $k_f = p_3/N_f$, and $k_t = p_1/N_t$. Then we compute

$$\mathcal{P} = \grave{\mathcal{R}} \times_1 \boldsymbol{D}_{p_1} \times_2 \boldsymbol{D}_{p_2} \times_3 \boldsymbol{D}_{p_3}^{\mathrm{H}} \times_4 \boldsymbol{D}_{p_4}, \tag{16}$$

where $\boldsymbol{D}_{p_r}$ is the $p_r \times p_r$ DFT matrix. The 4-D periodogram is obtained as

$$S(i_1, i_2, i_3, i_4) = \frac{1}{M_x M_y N_f N_t} |\mathcal{P}_{i_1,i_2,i_3,i_4}|^2, \tag{17}$$

where $\mathcal{P}_{i_1,i_2,i_3,i_4}$ is the (i_1, i_2, i_3, i_4)-th element of $\mathcal{P}$ and we have $i_1 \in \{1, \cdots, p_1\}$, $i_2 \in \{1, \cdots, p_2\}$, $i_3 \in \{1, \cdots, p_3\}$, and $i_4 \in \{1, \cdots, p_4\}$. Finally, the computational complexity of the 4-D periodogram is dominated by equation (16), which is given by $\mathcal{O}(p_1\, p_2\, p_3\, p_4(p_1 + p_2 + p_3 + p_4))$. Note that an adaptive implementation of (16) introduced in Section 3.3.2 of [3] can further reduce the overall computational complexity.

D. 4-D WIDEBAND UNITARY TENSOR-ESPRIT

In this section we introduce a closed-form multidimensional high-resolution parameter estimation method, which is based on the R-D Unitary Tensor-ESPRIT algorithm in [29]. 4-D Unitary Tensor-ESPRIT is a real-valued Tensor-ESPRIT algorithm that has a lower computationally complexity and a better performance compared to Standard Tensor-ESPRIT that is based on a complex-valued tensor decomposition [29], [37]. Next, we briefly describe how to extend the R-D Unitary Tensor-ESPRIT algorithm to our wideband problem.

First, define $\bar{f}_1 = -2\tau_h \Delta_f$ and $\bar{f}_2 = 2\frac{f_0 T_0}{c} \nu_h$. Assume that $\bar{f}_1 \in (-2, 0]$ and $\bar{f}_2 \in (-1, 1]$. Then we can interpret the exponential terms as a function of time delays τ_h and relative velocities ν_h as virtual uniform linear arrays (ULAs) with spatial frequencies $\bar{f}_1$ and $\bar{f}_2$, respectively.

Since ESPRIT-type algorithms require more than one snapshot, we apply 4-D smoothing and create a fifth dimension. We rearrange the measurements $\tilde{\mathcal{R}}^i$ in (10a) (and that, strictly speaking, corresponds to one large snapshot) in such a way that distinct parts of the measurements are treated as different snapshots. First, let us define $L = L_1\, L_2\, L_3\, L_4$ and $M_r = Z - L_r + 1$, where $Z \in \{M_x, M_y, N_f, N_t\}$. Then, we perform 4-D smoothing that can be expressed as

$$\begin{aligned} &\left(\tilde{\mathcal{R}}_{\mathrm{ss}}\right)_{(:,:,:,:,\ell_1 L_2 L_3 L_4 + \ell_2 L_3 L_4 + \ell_3 L_4 + \ell_4)} \\ &\quad = \tilde{\mathcal{R}}^i_{(\ell_1:\ell_1+M_1,\ell_2:\ell_2+M_2,\ell_3:\ell_3+M_3,\ell_4:\ell_4+M_4)}, \\ &\qquad\qquad \forall \ell_r \in \{0, \ldots, L_r - 1\} \end{aligned} \tag{18}$$

where the notation $x : y$ in the index denotes the selection of elements with indices between x and y (Matlab-like notation). As a result, a tensor $\tilde{\mathcal{R}}_{\mathrm{ss}}$ of size $M_1 \times M_2 \times M_3 \times M_4 \times L$ is obtained by stacking the L tensors in (18) along the 5-th dimension. Alternatively, the 4-D smoothing operation can be defined in terms of selection matrices, cf. Section VI of [29].

Next, we define the forward-backward averaged version of the tensor $\tilde{\mathcal{R}}_{\mathrm{ss}}$ as

$$\begin{aligned} \mathcal{F} &= \left[\tilde{\mathcal{R}}_{\mathrm{ss}} \sqcup_5 \tilde{\mathcal{R}}_{\mathrm{ss}}^{\Pi}\right], \quad \text{where} \\ \tilde{\mathcal{R}}_{\mathrm{ss}}^{\Pi} &= \left[\tilde{\mathcal{R}}_{\mathrm{ss}} \times_1 \boldsymbol{\Pi}_{M_1} \times_2 \boldsymbol{\Pi}_{M_2} \times_3 \boldsymbol{\Pi}_{M_3} \times_4 \boldsymbol{\Pi}_{M_4} \times_5 \boldsymbol{\Pi}_L\right] \end{aligned}$$

Then the tensor $\mathcal{F} \in \mathbb{C}^{M_1 \times M_2 \times M_3 \times M_4 \times L}$ is a centro-Hermitian tensor. The proof is straightforward according to Lemma 3 in [29].

Therefore we can map the centro-Hermitian tensor $\mathcal{F}$ into a real-valued tensor $\mathcal{F}_{\mathrm{r}}$ by computing [29]

$$\mathcal{F}_{\mathrm{r}} = \mathcal{F} \times_1 \boldsymbol{Q}_{M_1} \times_2 \boldsymbol{Q}_{M_2} \times_3 \boldsymbol{Q}_{M_3} \times_4 \boldsymbol{Q}_{M_4} \times_5 \boldsymbol{Q}_{2L}, \tag{19}$$

where the matrix $\boldsymbol{Q}_m$ is assumed to be left-$\boldsymbol{\Pi}$-real. According to [29], the rest of the 4-D Wideband Unitary Tensor-ESPRIT algorithm consists of three steps, i.e., estimating the real-valued signal subspace, solving the linear 4-D shift invariance equations using, for example, least squares (LS), and computing the simultaneous Schur decomposition (SSD) or joint eigenvalue decomposition (JEVD) to obtain automatically paired frequencies u_h, v_h, $\bar{f}_1$, and $\bar{f}_2$. Except for the tensor-based signal subspace estimation step, the implementation of 4-D Wideband Unitary Tensor-ESPRIT is the same as in [29]. To avoid the computation of the truncated core tensor of the HOSVD of the real-valued tensor $\mathcal{F}_r$, we use the following relationship between the SVD-based and the HOSVD-based subspace estimates [38], [39],

$$\begin{aligned} \left[\hat{\mathcal{U}}_{\mathrm{s}}\right]^{\mathrm{T}}_{(5)} = \Big(&(\hat{\boldsymbol{U}}_{\mathrm{s},1} \hat{\boldsymbol{U}}^{\mathrm{H}}_{\mathrm{s},1}) \otimes (\hat{\boldsymbol{U}}_{\mathrm{s},2} \hat{\boldsymbol{U}}^{\mathrm{H}}_{\mathrm{s},2}) \\ &\otimes (\hat{\boldsymbol{U}}_{\mathrm{s},3} \hat{\boldsymbol{U}}^{\mathrm{H}}_{\mathrm{s},3}) \otimes (\hat{\boldsymbol{U}}_{\mathrm{s},4} \hat{\boldsymbol{U}}^{\mathrm{H}}_{\mathrm{s},4}) \Big) \cdot \hat{\boldsymbol{U}}_{\mathrm{s}}, \end{aligned} \tag{20}$$

where $\hat{\mathcal{U}}_{\mathrm{s}} \in \mathbb{R}^{M_1 \times M_2 \times M_3 \times M_4 \times H}$ and $\hat{\boldsymbol{U}}_{\mathrm{s}} \in \mathbb{R}^{M_1\, M_2\, M_3\, M_4 \times H}$ represent the tensor-based and the matrix-based signal subspace estimate, respectively. The matrices $\hat{\boldsymbol{U}}_{\mathrm{s},r} \in \mathbb{R}^{M_r \times H}$ and $\hat{\boldsymbol{U}}_{\mathrm{s}}$ consist of the first H left singular vectors of the r-mode unfolding $[\mathcal{F}_{\mathrm{r}}]_{(r)}$ ($r \in \{1, 2, 3, 4\}$) and $[\mathcal{F}_{\mathrm{r}}]^{\mathrm{T}}_{(5)}$, respectively. Therefore, these matrices can be obtained by computing the truncated SVDs of the corresponding unfoldings, each of which yield a computational complexity of order $\mathcal{O}(M_1 M_2 M_3\, M_4\, LH)$. Hence, the computational complexity of our proposed 4-D Wideband Unitary Tensor-ESPRIT is dominated by computing equation (20), which has the order of $\mathcal{O}(M_1^2 M_2^2\, M_3^2\, M_4^2\, H)$.

To summarize, the proposed interpolation based coherent parameter estimation framework is described in Algorithm 1.

It should be noted here that, in general, the interpolation errors of piece-wise polynomial interpolation techniques increase if the harmonic frequencies are increased with respect to the sampling frequencies in the respective dimension (in other words, if the relative digital frequencies

Algorithm 1 4-D Wideband Coherent Parameter Estimation Framework

```
Input: $y_{m_x,m_y,n_f}[n_t]$, $s_{n_f}[n_t]$, $\forall m_x, m_y, n_f, n_t$. If the 4-D periodogram is used, set $p_1, p_2, p_3$, and $p_4$. If 4-D Unitary Tensor-ESPRIT is used, set $L_1$, $L_2$, $L_3$, and $L_4$.
Main step:
Obtain $\tilde{\mathcal{R}}^i$ via piece-wise polynomial interpolation methods using (10a) and (12a) or (12b).
if 4-D periodogram then
    Compute (16) and (17).
else if 4-D Wideband Unitary Tensor-ESPRIT then
    Obtain $\tilde{\mathcal{R}}_{\mathrm{ss}}$ using (18)
    Estimate the tensor-based signal subspace $\hat{\mathcal{U}}_{\mathrm{s}}$ using (20)
    Compute the LS solution of the shift invariance equation as in [29]
    Compute the SSD to obtain automatically paired spatial frequencies $u_h$, $v_h$, $\bar{f}_1$, and $\bar{f}_2$ as in [29]
end if
Output: $\tau_h$, $\nu_h$, $\phi_h$, and $\theta_h$, $\forall h$.
```

in the respective dimensions are high). To avoid these errors, one could use oversampling such that these frequencies are kept small for any possible values of the parameters of interest (relative velocity and DoAs). Windowing can also decrease interpolation errors, especially for the Shannon-Whittaker interpolation. But it cannot be used when ESPRIT-type algorithms are applied, because it will destroy the shift invariant structure of the measurements.

IV. SIMULATION RESULTS

In this section, the proposed interpolation based coherent parameter estimation framework is evaluated using Monte Carlo simulations. During our simulations, the following assumptions are made: 1) the radar targets are considered as point scatterers; 2) we use a free space path loss model; 3) there is no clutter in the system. For simplicity, the simulations are carried out directly using the models in (2), denoted as "Wideband" ("Wbd."), and (4), denoted as "Narrowband" ("Nbd.") model, respectively. By using those models we assume that there is no inter-carrier interference due to the non-zero Doppler shift of the targets. This provides better insights into the performance of the interpolation algorithms.

The carrier frequency $f_c = f_0 + \frac{N_f-1}{2}\Delta_f$, as depicted in Figure 3, varies across simulations in order to unveil the influence of the fractional bandwidth $B_{\mathrm{fr}} = \frac{B}{f_c} = \frac{N_f \Delta_f}{f_c}$. Three scenarios are simulated with $f_c = 30$ GHz, 3 GHz and 0.3 GHz. The OFDM symbol duration is set to $T_0 = 2.7\,\mu$s. The FFT size is $N_{\mathrm{fft}} = 64$ and we set $N_f = N_{\mathrm{fft}}$. The system bandwidth is $B = 86.4$ MHz for $\Delta_f = 1.35$ MHz and $B = 83.2$ MHz for $\Delta_f = 1.3$ MHz. The physical antenna spacing is chosen as $\Delta_x = \Delta_y = \frac{c}{8 f_{N_f-1}}$, which results in oversampling in the spatial domains. Each training period consists of $N_t = 10$ OFDM symbols. The URA is of size $M_x \times M_y = 10 \times 10$. The transmit power is equal to $P_t = 40$ dBm. When the R-D periodogram is used, we set $k_x = k_y = k_f = k_t = 5$. When R-D Wideband Unitary Tensor-ESPRIT is used, we set $L_1 = L_2 = 1$, $L_3 = 55$ and $L_4 = 3$, which leads to $\tilde{\mathcal{R}}_{ss} \in \mathbb{C}^{10\times 8\times 10\times 10\times 165}$. In all simulations, additive zero-mean circularly symmetric complex Gaussian (ZMCSCG) noise is used. The simulation results are averaged over 1000 realizations.

To avoid separate plots for range, relative velocity, azimuth, and elevation we use a performance evaluation metric defined as a joint RMSE for all estimated parameters. This weighted $\mathrm{RMSE_{tot}}$ takes into account errors in all estimated parameters:

$$\begin{aligned}\mathrm{RMSE_{tot}} &= \sqrt{\sum_{r=1}^{4} w_{(r)}^2 \frac{1}{H}\mathbb{E}\left\{\sum_{h=1}^{H}(x_h^{(r)} - \hat{x}_h^{(r)})^2\right\}} \\ &= \sqrt{\sum_{r=1}^{4} w_{(r)}^2 \frac{1}{H}\sum_{k=1}^{K}\sum_{h=1}^{H}(x_h^{(r)} - \hat{x}_h^{(r,k)})^2}. \qquad (21)\end{aligned}$$

where $x_h^{(r)} \in \{d_h, \nu_h, u_h, v_h\}$ and $\hat{x}_h^{(r,k)}$ is an estimate of $x_h^{(r)}$ in the k-th trial ($1 \leq k \leq K$). Since the estimated parameters have different units and orders of magnitude, we define the weighting coefficients $w_{(r)} = [10^{-4}$ 1/m, 10^{-5} s/m, 1 ,1]. These coefficients have been chosen empirically based on the particular values of the averaged errors obtained during our simulations to balance the contribution from all four estimated parameters into the joint performance metric $\mathrm{RMSE_{tot}}$.

In the first simulation, we have two targets, i.e., $H = 2$, and our goal is to study the spatial resolution provided by the proposed algorithms. We set $\phi_1 = \phi_2 = 135°$ and $\theta_1 = \theta_2 = 65°$, and velocities $v_{x,1} = v_{x,2} = 40$ m/s, $v_{y,1} = v_{y,2} = v_{z,1} = v_{z,2} = 0$ m/s, where $v_{x,h}$, $v_{y,h}$ and $v_{z,h}$ are projections of the absolute speed on Euclidean coordinates. The distance between the radar and the first target is $d_1 = 50$ m while the distance between the radar and the second target d_2 varies from 30 m to 70 m during the simulation. Let "Per." and "UTE" denote the 4-D periodogram and the 4-D Unitary Tensor-ESPRIT algorithm, respectively. Let "linear" and "spline" represent the linear and spline interpolation, "SW" represents Shannon-Whittaker interpolation, while "s7" and "s10" refer to the higher-order spline interpolation with an order equal to 7 or 10, respectively. Finally, "D" denotes the use of the additional "denoising" pre-processing step, described in Subsection III-B.

Since the fractional bandwidth is varied by changing the carrier frequency, the received SNR, defined in (22), also changes. The received SNR for the first target is defined as

$$\mathrm{SNR}_{\mathrm{Rx},1} = 10\log_{10}\left(\frac{P_{\mathrm{Tx}} L_1}{F k_B T B}\right), \qquad (22)$$

where P_{Tx} is the transmitted power in Watts (10 Watts), k_B is the Boltzmann constant, $T = 290$ K is the receiver temperature, B is the bandwidth and $L_1 = \tilde{k}_1^2$ is the free space pathloss coefficient of the first target, where $\tilde{k}_h$ was defined in Section II.

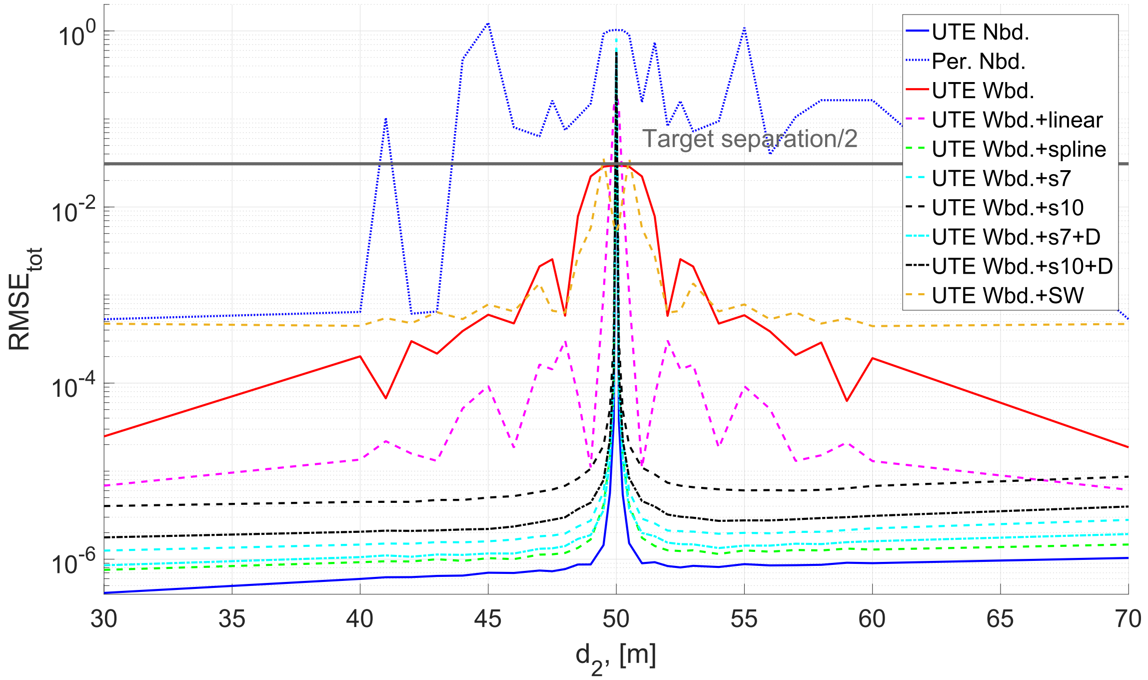

FIGURE 4. Total RMSE_{tot} vs. the distance to the second target. The distance to the second target d_2 is varied from 30 to 70 meters, while the distance to the first target d_1 is held fixed to 50 meters. Fractional bandwidth $B_{\text{fr}} \approx 28$ % and $\text{SNR}_{\text{Rx}} \approx 70$ dB.

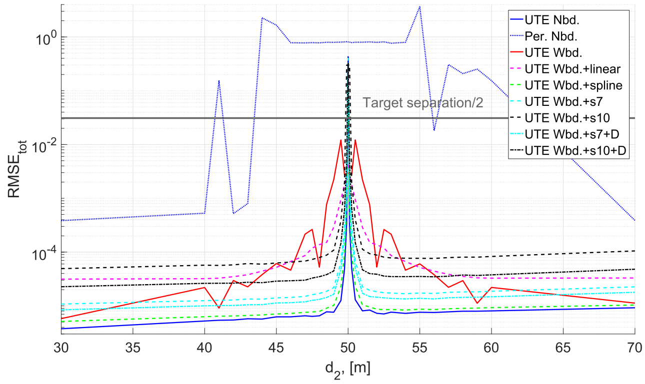

FIGURE 5. Total RMSE_{tot} vs. the distance to the second target. The distance to the second target d_2 is varied from 30 to 70 meters, while the distance to the first target d_1 is held fixed to 50 meters. Fractional bandwidth $B_{\text{fr}} \approx 2.8$ % and $\text{SNR}_{\text{Rx}} \approx 50$ dB.

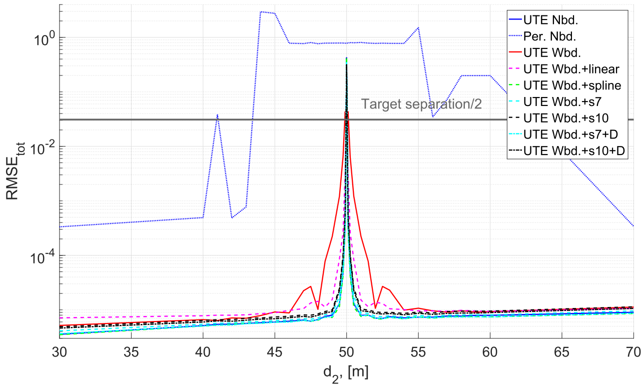

FIGURE 6. Total RMSE_{tot} vs. the distance to the second target. The distance to the second target d_2 is varied from 30 to 70 meters, while the distance to the first target d_1 is held fixed to 50 meters. Fractional bandwidth $B_{\text{fr}} \approx 0.28$ % and $\text{SNR}_{\text{Rx}} \approx 50$ dB.

To compensate those changes, we use different noise figures F in different simulations, resulting in different $\text{SNR}_{\text{Rx},1}$ at a distance of 50 meters. In Figure 4 we get $\text{SNR}_{\text{Rx},1} \approx 70$ dB, in Figure 5 $\text{SNR}_{\text{Rx},1} \approx 50$ dB, and in Figure 6 we get $\text{SNR}_{\text{Rx},1} \approx 50$ dB.

From Figures 4, 5, and 6 it is observed that distortions caused by the wideband data model (red curve) cause some performance degradation when the target separation is small. The difference in performance between the narrowband data model (blue curve) and the wideband data model (red curve) increases with B_{fr} (Figures 4 and 5) or $\text{SNR}_{\text{Rx},1}$ (Figure 4). The best choice for this setup is cubic spline interpolation (green curve), which uses polynomials of degree 3 for the interpolation. But the performance for the splines with higher-order (light-blue and black curves) is worse, which shows that they are sensitive to additive noise. Although it could be improved via the "denoising" pre-processing step described in Subsection III-B (dash-dotted light-blue curve and dash-dotted black curve, respectively), cubic spline interpolation still outperforms them in this scenario. The performance of the linear interpolation (pink curve) shows that choosing a low interpolation order results in a poorer performance due to a larger interpolation error.

Additionally, from Figures 4, 5, and 6 we observe how high-resolution 4-D Unitary Tensor-ESPRIT outperforms

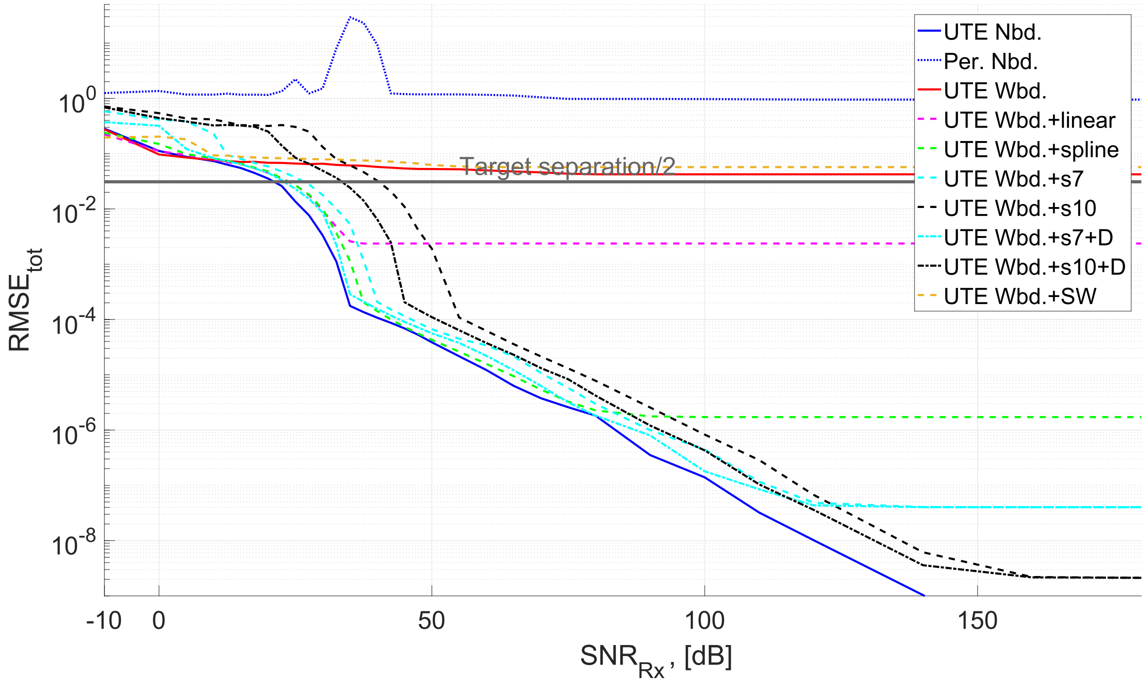

FIGURE 7. Total $\mathrm{RMSE_{tot}}$ vs. received SNR. The received SNR (computed for the first target, (22)) is varied from −10 dB to 170 dB. Fractional bandwidth $B_{\mathrm{fr}} \approx 28$ %.

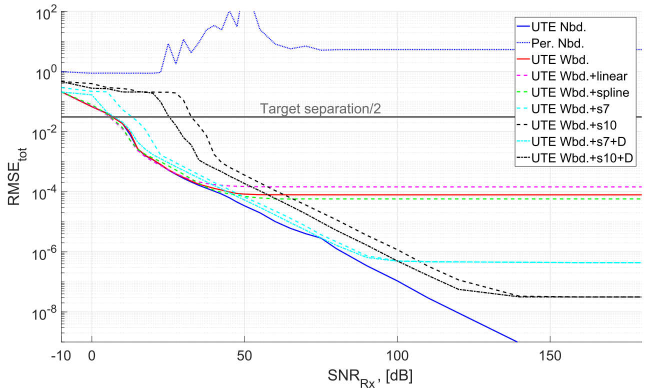

FIGURE 8. Total $\mathrm{RMSE_{tot}}$ vs. received SNR. The received SNR (computed for the first target, (22)) is varied from −10 dB to 170 dB. Fractional bandwidth $B_{\mathrm{fr}} \approx 2.8$ %.

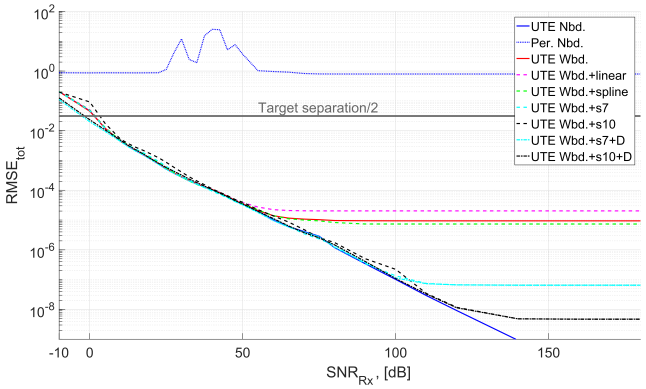

FIGURE 9. Total $\mathrm{RMSE_{tot}}$ vs. received SNR. The received SNR (computed for the first target, (22)) is varied from −10 dB to 170 dB. Fractional bandwidth $B_{\mathrm{fr}} \approx 0.28$ %.

4-D periodogram in terms of the resolution, even if the narrowband data model is used for the periodogram.

In the second simulation, we consider five fixed targets, i.e., $H = 5$, and the estimation error is plotted as a function of the received $\mathrm{SNR}_{\mathrm{Rx},1}$ of the first target at a distance $d_1 = 80$ m, which is altered via changing the noise figure F.

The five targets are chosen to be close to each other: $d_h \in \{80, 85, 90, 95, 100\}$ m, $\phi_h \in \{82°, 86°, 90°, 94°, 98°\}$, $\theta_h \in \{60°, 63°, 66°, 69°, 72°\}$ with $\nu_{y,h} = 40$ m/s and $\nu_{x,h} = \nu_{z,h} = 0$ m/s for all $h \in \{1, \cdots, 5\}$. Although the absolute velocities of the targets are the same, their velocities relative to the receiver are different and equal to $\nu_h \in \{-19.8, -18.1, -16.3, -14.3, -12.2\}$ m/s. The total RMSE in (21) is computed using estimates of the directional cosines u_h and v_h. In this scenario they are as follows: $u_h \in \{0.07, 0.032, 0, -0.025, -0.043\}$, $v_h \in \{0.5, 0.453, 0.407, 0.358, 0.306\}$.

Figures 7, 8, and 9 depict the results of the second simulation. The grey horizontal line refers to errors that are equal to half of the target separation, which is computed using the definition of the total RMSE, where half of the target separations are used instead of the parameter errors in equation (21). Periodogram based solutions fail to resolve such closely spaced targets. For a low fractional bandwidth (Figure 9), the gain from the use of interpolation pre-processing appears only in the high SNR regimes, e.g., for $\mathrm{SNR}_{\mathrm{Rx},1} > 65$ dB, and linear interpolation is even worse than not using any

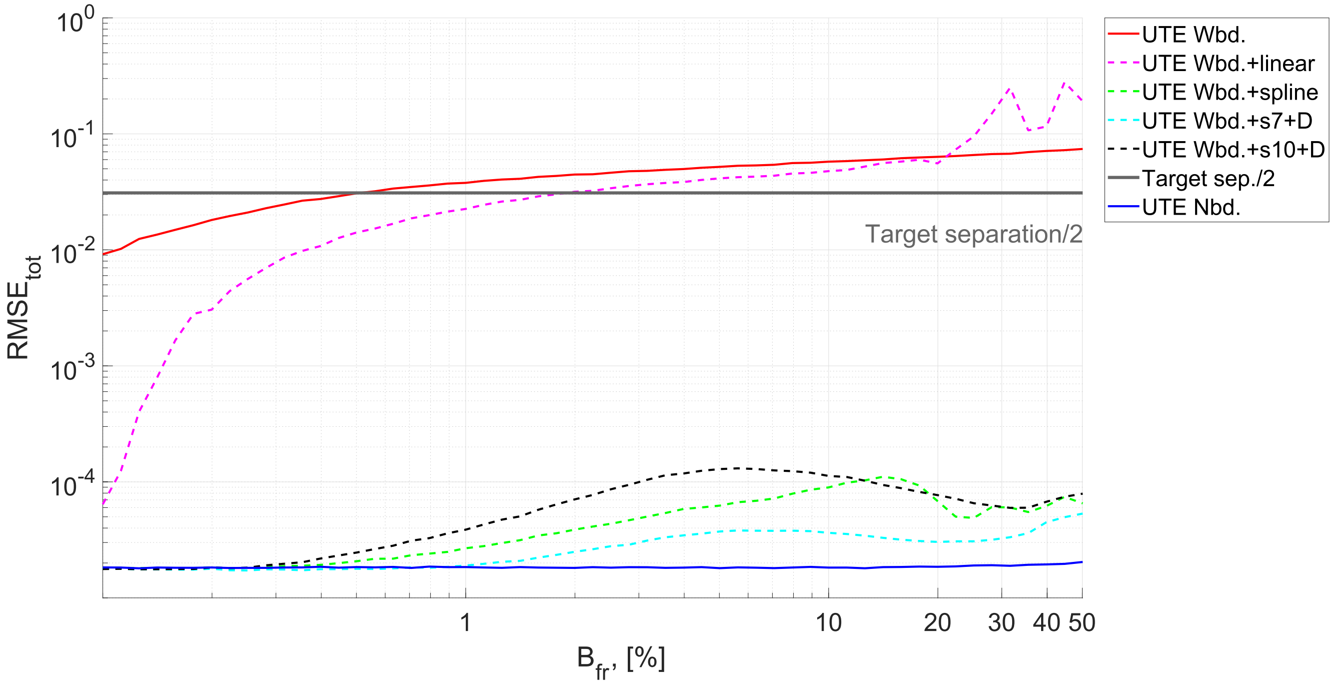

FIGURE 10. Total RMSE$_{\text{tot}}$ vs. the fractional bandwidth B_{fr}. Fractional bandwidth B_{fr} is varied from 0.1 % to 50 %. This variation is achieved by changing the carrier frequency f_c.

interpolation at all (red curve), since it introduces high interpolation errors. Since there are always residual interpolation errors, error floors exist for all algorithms in case of the wideband model (1) even when the received SNR$_{\text{Rx},1}$ is large. The higher-order spline interpolation allows to reduce interpolation errors, although it is less robust, which can be observed from Figures 7 and 8. The proposed 4-D Wideband Unitary Tensor-ESPRIT combined with interpolation preprocessing is able to restore the performance of narrowband algorithms even in such an extreme scenario with $B_{\text{fr}} = 28$ % (Figure 7). If no interpolation pre-processing is used (red curve), the algorithm fails to resolve the targets, providing an error that is higher than the target separation. Therefore, the interpolation order allows a trade-off between the performance in the high and the low SNR regimes. The performance for the higher-order splines can be improved by using the additional "denoising" pre-processing step described in Subsection III-B. As already mentioned, this step allows to reduce the influence of the noise on the system, except for cases with high SNRs, but its effect is only seen in case of interpolation with splines of a higher order. This is due to the vulnerability of those techniques to perturbations, which is also observed in the simulation results. It is worth mentioning that there is no benefit to choose interpolation orders larger than the number of samples in the respective dimension [33]. The best performance in this setup is achieved by using an interpolation order of 7 with the additional "denoising" step.

The last simulation investigates the RMSE performance versus the fractional bandwidth B_{fr}, which is varied by changing the carrier frequency f_c. It should be noted that the SNR will also change along with the fractional bandwidth, i.e. SNR$_{\text{Rx},1}$ will change from 21.5 dB at $f_c = 57.6$ GHz to 72 dB at $f_c = 172.8$ MHz. To make the comparison clearer, we fix the received SNR of the first target SNR$_{\text{Rx},1} = 45$ dB by recomputing the noise figure F for each value of the carrier frequency f_c:

$$F = 10\log_{10}\left(\frac{P_{\text{Tx}}L_1}{\text{SNR}_{\text{Rx},1}k_B TB}\right) \tag{23}$$

For this simulation, we use slightly different target parameters. Again, five targets are chosen to be close to each other: $d_h \in \{60, 65, 70, 75, 80\}$ m, $\phi_h \in \{42^\circ, 46^\circ, 50^\circ, 54^\circ, 58^\circ\}$, $\theta_h \in \{60^\circ, 63^\circ, 66^\circ, 69^\circ, 72^\circ\}$ with $v_{y,h} = 40$ m/s and $v_{x,h} = v_{z,h} = 0$ m/s for all $h \in \{1, \cdots, 5\}$. The results are presented in Figure 10. It can be observed how the performance gain from interpolation pre-processing increases when a high fractional bandwidth is present and the SNR increases. For the chosen SNR, when the fractional bandwidth increases beyond 1 %, the targets are not resolved without interpolation preprocessing. Since the SNR is kept constant the performance in the narrowband system is constant as well, but the performance in wideband system degrades very rapidly and exceeds the target separation soon after the fractional bandwidth becomes larger than 1 %. It can also be observed that linear interpolation is effective only up to 2 % fractional bandwidth and fails to resolve targets beyond that limit, while the best performance is achieved with 7-th order spline interpolation. The worse performance of the 10-th order spline can be explained by its vulnerability to additive noise, while the cubic spline lacks degrees of freedom to precisely approximate the signal samples.

V. CONCLUSION

In this paper, we have studied a wideband OFDM based joint radar and communication system. The wideband assumption results in incoherent signals on different subcarriers. To reduce the incoherence we propose an interpolation based coherent parameter estimation framework.

First, the wideband system model is converted into an approximately equivalent narrowband model by using piecewise polynomial interpolation methods of different orders. Linear interpolation is chosen due to its lowest computational complexity, while cubic spline interpolation is used due to its low interpolation error. Splines with higher-orders have also been investigated.

Then the multidimensional parameter estimation algorithms, i.e., a benchmark algorithm based on the 4-D periodogram and the proposed 4-D Wideband Unitary Tensor-ESPRIT, are applied to provide accurate estimates of the parameters of the dominant radar targets. The simulation results show that interpolation based coherent signal subspace estimation is able to enhance the wideband signal subspace estimate, which, in turn, improves the estimation accuracy. This method allows the application of multidimensional narrowband parameter estimation techniques in wideband systems.

It can be observed that the gain obtained by using the interpolation based coherent estimation approach depends on the scenario, the signal-to-noise ratio, and the fractional bandwidth. It is shown that the Shannon-Whittaker interpolation does not perform well for signals with a few samples, resulting in high interpolation errors. In the low SNR regime, the interpolation preprocessing is not needed since the estimation error is dominated by additive noise distortions.

When the fractional bandwidth is small and the SNR is high, the cubic spline interpolation and interpolation with higher-order polynomials provide a gain when compared to the direct application of the narrowband algorithm as well as linear interpolation. As the fractional bandwidth increases, narrowband algorithms fail to resolve closely spaced targets, and interpolation becomes necessary. If the SNR is very high (more than 70 dB for the given simulation parameters and scenarios), it also becomes profitable to increase the order of the interpolating polynomials, which will improve the estimation accuracy. An additional "denoising" step can improve the performance for the higher-order spline interpolation techniques. In general, we recommend to use interpolation pre-processing techniques to resolve closely spaced targets in the high SNR regime, or when the fractional bandwidth is larger than 20-30 %. A brief summary of the recommendations on using interpolation pre-processing is presented in Table 1. Note that the interpolation pre-processing step can also be used in other applications with a large fractional bandwidth, such as, for example, audio source localization with microphone arrays.

TABLE 1. Recommendations on using interpolation pre-processing.

	Low Fractional Bandwidth (< 1 %)	**High Fractional Bandwidth** (> 10 %)
Low SNR (up to 40 dB)	No interpolation is needed due to noise	
High SNR (40 to 70 dB)	Cubic and higher-order splines	Cubic splines
Extremely high SNR (more than 70 dB)	Higher-order splines + "Denoising"	

APPENDIX A
LINEAR INTERPOLATION MATRICES

In the appendices we show that both linear and spline interpolation can be expressed as a simple multi-linear transformation along each mode of the measurement tensor, as shown in equations (12a) and (12b).

Piecewise linear interpolation, or often called linear interpolation, belongs to the family of piecewise polynomial interpolation techniques. It uses interpolating polynomials of degree 1, or, in other words, straight lines.

To simplify the notation, we define $y(n)$ to be a sampled sequence of size N, i.e., $n \in \{0, \ldots, N-1\}$. This sequence is then stacked into the vector $\boldsymbol{y} \in \mathbb{C}^N$. For example, this could be any n-mode vector of the tensor $\breve{\mathcal{R}}_{n_f}$ (defined in Subsection III-A) corresponding to time or one of the spatial measurement dimensions, for example:

$$\begin{aligned} \boldsymbol{y}^t_{m_x,m_y} &= \left(\breve{\mathcal{R}}_{n_f}\right)_{(:,m_x,m_y)} \\ \boldsymbol{y}^x_{n_t,m_x} &= \left(\breve{\mathcal{R}}_{n_f}\right)_{(n_t,m_x,:)} \\ \boldsymbol{y}^y_{n_t,m_y} &= \left(\breve{\mathcal{R}}_{n_f}\right)_{(n_t,:,m_y)} \end{aligned} \tag{25}$$

In any of those cases, the sequence $\boldsymbol{y}$ has the original sampling interval. In case of time, it is T_0, and in case of spatial sampling, it is Δ_x or Δ_y. We denote this original sampling interval as X_0, where $X_0 \in \{T_0, \Delta_x, \Delta_y\}$ and the corresponding continuous argument as x. This means that $\boldsymbol{y}$ contains samples of a continuous function $y(x)$ with sampling interval X_0, and the first sampling point is located at $x = 0$.

Next, we want to interpolate the signal or resample it to obtain the same number of samples N of $y(x)$ but using a smaller sampling interval $X_i < X_0$, or a larger sampling frequency $f_i^s > f_0^s$.

Let us denote the interpolated sequence of values as $y^I(m)$, where $m \in \{0, \ldots, N-1\}$, and assume that the first sample of the new sequence is also made for $x = 0$. Then we get

$$y^I(m) = y(n)\frac{(n+1)X_0 - mX_i}{X_0} + y(n+1)\frac{mX_i - nX_0}{X_0}, \tag{26}$$

where $mX_i \in (nX_0, (n+1)X_0]$, or by using the conversion factor $\Delta = \frac{X_i}{X_0}$

$$y^i(m) = y(n)\Big(n + 1 - m\Delta\Big) + y(n+1)\Big(m\Delta - n\Big), \tag{27}$$

where $m\Delta \in (n, n+1]$. If the common sampling point is in the middle of the overall sampling interval, i.e., the sampling

$$y^i(m) = \underbrace{\begin{bmatrix} 0 & \dots & 0 & 1-\{m\Delta\} & \{m\Delta\} & 0 & \dots & 0 \end{bmatrix}}_{\boldsymbol{l}^T_{m,\Delta}} \begin{bmatrix} y(0) \\ \vdots \\ y(n) \\ y(n+1) \\ \vdots \\ y(N-1) \end{bmatrix} = \boldsymbol{l}^T_{m,\Delta} \cdot \boldsymbol{y} \tag{24}$$

sequences are aligned such that the point $x = \frac{(N-1)X_0}{2}$ is in the middle of both of them, then mX_i should be replaced by $mX_i - \frac{(N-1)}{2}(X_0 - X_i)$ in (26) or $m\Delta$ should be replaced by $m\Delta - \frac{(N-1)}{2}(1-\Delta)$ in (27). This also applies to the other equations. In the sequel, we assume $x = 0$ as the common sampling point for notational simplicity.

It is easy to show that since $m\Delta \in (n, n+1]$ we get

$$n = \lfloor m\Delta \rfloor, \quad n+1 = \lceil m\Delta \rceil \tag{28}$$

where $\lfloor a \rfloor$ and $\lceil a \rceil$ denote the floor and the ceiling operations, respectively.

If we insert the definition in (28) into (27), we get

$$y^i(m) = y(n)\Big(1 - \Big\{m\Delta\Big\}\Big) + y(n+1)\Big(\Big\{m\Delta\Big\}\Big), \tag{29}$$

where $mX_i \in (nX_0, (n+1)X_0]$ and $\{a\}$ denotes the fractional part of a. From this equation, we can observe that the interpolated value depends on the index m and the conversion factor Δ, and it is linear in the data (or in $y(n)$).

Next, we can express equation (29) as a scalar product between the vector $\boldsymbol{l}_{m,\Delta} \in \mathbb{R}^N$ and the vector $\boldsymbol{y}$, as indicated in equation (24), as shown at the top of this page, where the vector $\boldsymbol{l}_{m,\Delta} \in \mathbb{R}^N$ depends on sample index m and the conversion factor Δ.

We stack all $\boldsymbol{l}_{m,\Delta}$ into one linear interpolation matrix $\boldsymbol{L}_{\Delta,N}$

$$\boldsymbol{L}_{\Delta,N} = \begin{bmatrix} \boldsymbol{l}^T_{0,\Delta} \\ \vdots \\ \boldsymbol{l}^T_{m,\Delta} \\ \vdots \\ \boldsymbol{l}^T_{N-1,\Delta} \end{bmatrix} \in \mathbb{R}^{N \times N} \tag{30}$$

such that we finally obtain

$$\boldsymbol{y}^l = \boldsymbol{L}_{\Delta,N} \cdot \boldsymbol{y} \tag{31}$$

where the samples $y^l(m)$ are stacked into $\boldsymbol{y}^l$, where $m \in \{0, \dots, N-1\}$. Thus, the $\boldsymbol{L}_{\Delta,N}$ is fully determined by the conversion factor Δ, the number of samples N, and the common data point (for this example it is $x = 0$). The matrix $\boldsymbol{L}_{\Delta,N}$ is used in (12a).

APPENDIX B
SPLINE INTERPOLATION MATRICES

As in the previous appendix, we show that spline interpolation can also be expressed as a simple multi-linear transformation along each mode of the measurement tensor, as shown in equations (12a) and (12b).

Cubic spline interpolation also belongs to the family of piecewise polynomial interpolation techniques that use polynomials of degree 3 (or fourth-order splines).

Following the same notation as in Appendix A, we first define the slopes of the interpolation polynomial

$$d(n) = \frac{dy^s(x)}{dx}\bigg|_{x=nX_0} \tag{34}$$

where $n \in \{0, \dots, N-1\}$, or in vector form

$$\boldsymbol{d} = \begin{bmatrix} d(0) & d(1) & \dots & d(N-1) \end{bmatrix}^T \in \mathbb{C}^N \tag{35}$$

where $y^s(x)$ denotes the continuous interpolating function which produces a resampled sequence $y^s(m)$ ($m \in \{0, \dots, N-1\}$) using the sampling interval X_i.

The interpolating piece-wise polynomial function is defined as

$$\begin{aligned} y^i(x) = {} & y(n)\frac{X_0^3 - 3X_0(x-nX_0)^2 + 2(x-nX_0)^3}{X_0^3} \\ & + y(n+1)\frac{3X_0(x-nX_0)^2 - 2(x-nX_0)^3}{X_0^3} \\ & + d(n)\frac{(x-nX_0)(x-(n+1)X_0)^2}{X_0^2} \\ & + d(n+1)\frac{(x-nX_0)^2(x-(n+1)X_0)}{X_0^2}, \\ & \text{for } x \in (nX_0, (n+1)X_0] \end{aligned} \tag{36}$$

Again, assuming $x = 0$ as the common sampling point, the resampled sequence is then expressed in equation (32), as shown at the top of the next page, or by using the conversion factor Δ

$$\begin{aligned} y^i(m) = {} & y(n)\big(1 - 3(m\Delta - n)^2 + 2(m\Delta - n)^3\big) \\ & + y(n+1)\big(3(m\Delta - n)^2 - 2(m\Delta - n)^3\big) \\ & + d(n)X_0(m\Delta - n)(m\Delta - n - 1)^2 \\ & + d(n+1)X_0(m\Delta - n)^2(m\Delta - n - 1), \\ & \text{for } m\Delta \in (n, n+1] \end{aligned} \tag{37}$$

and using $m\Delta - n = \{m\Delta\}$ (fractional part), we get

$$\begin{aligned} y^i(m) = {} & y(n)\big(1 - 3\{m\Delta\}^2 + 2\{m\Delta\}^3\big) \\ & + y(n+1)\big(3\{m\Delta\}^2 - 2\{m\Delta\}^3\big) \\ & + d(n)X_0\{m\Delta\}(\{m\Delta\} - 1)^2 \\ & + d(n+1)X_0\{m\Delta\}^2(\{m\Delta\} - 1) \end{aligned} \tag{38}$$

$$\begin{aligned} y^i(m) &= y(n)\frac{X_0^3 - 3X_0(mX_i - nX_0)^2 + 2(mX_i - nX_0)^3}{X_0^3} + y(n+1)\frac{3X_0(mX_i - nX_0)^2 - 2(mX_i - nX_0)^3}{X_0^3} \\ &\quad + d(n)\frac{(mX_i - nX_0)(mX_i - (n+1)X_0)^2}{X_0^2} + d(n+1)\frac{(mX_i - nX_0)^2(mX_i - (n+1)X_0)}{X_0^2}, \\ &\qquad \text{for } mX_i \in (nX_0, (n+1)X_0] \end{aligned} \tag{32}$$

$$\begin{aligned} y^i(m) &= \underbrace{\left[0 \ldots 0 \; 1 - 3\{m\Delta\}^2 + 2\{m\Delta\}^3 \; 3\{m\Delta\}^2 - 2\{m\Delta\}^3 \; 0 \ldots 0\right]}_{\boldsymbol{s}_{m,\Delta}^{(1)\,T}} \boldsymbol{y} \\ &\quad + X_0 \underbrace{\left[0 \ldots 0 \; \{m\Delta\}(\{m\Delta\} - 1)^2 \; \{m\Delta\}^2(\{m\Delta\} - 1) \; 0 \ldots 0\right]}_{\boldsymbol{s}_{m,\Delta}^{(2)\,T}} \boldsymbol{d} \\ &= \left(\boldsymbol{s}_{m,\Delta}^{(1)}\right)^T \cdot \boldsymbol{y} + X_0 \left(\boldsymbol{s}_{m,\Delta}^{(2)}\right)^T \cdot \boldsymbol{d} \end{aligned} \tag{33}$$

$$\underbrace{\begin{bmatrix} 1 & 2 & & & & \\ 1 & 4 & 1 & & & \\ & 1 & 4 & 1 & & \\ & & \ddots & \ddots & \ddots & \\ & & & 1 & 4 & 1 \\ & & & & 2 & 1 \end{bmatrix}}_{\boldsymbol{A} \in \mathbb{R}^{N \times N}} \underbrace{\begin{bmatrix} d(0) \\ d(1) \\ d(2) \\ \vdots \\ d(N-2) \\ d(N-1) \end{bmatrix}}_{\boldsymbol{d}} = \frac{3}{X_0} \underbrace{\begin{bmatrix} -5/6 & 4/6 & 1/6 & & & \\ -1 & 0 & 1 & & & \\ & -1 & 0 & 1 & & \\ & & \ddots & \ddots & \ddots & \\ & & & -1 & 0 & 1 \\ & & & -1/6 & -4/6 & 5/6 \end{bmatrix}}_{\boldsymbol{B} \in \mathbb{R}^{N \times N}} \underbrace{\begin{bmatrix} y(0) \\ y(1) \\ y(2) \\ \vdots \\ y(N-2) \\ y(N-1) \end{bmatrix}}_{\boldsymbol{y}} \tag{44}$$

---

which can be rewritten as the sum of two scalar products as shown in equation (33), as shown at the top of this page.

As before, we stack all $\boldsymbol{s}_{m,\Delta}^{(1)}$ and $\boldsymbol{s}_{m,\Delta}^{(2)}$ into two linear matrices $\boldsymbol{S}_{\Delta,N}^{(1)}$ and $\boldsymbol{S}_{\Delta,N}^{(2)}$

$$\begin{aligned} \boldsymbol{S}_{\Delta,N}^{(1)} &= \left[\boldsymbol{s}_{0,\Delta}^{(1)} \quad \ldots \quad \boldsymbol{s}_{N-1,\Delta}^{(1)}\right]^T \in \mathbb{R}^{N \times N} \\ \boldsymbol{S}_{\Delta,N}^{(2)} &= \left[\boldsymbol{s}_{0,\Delta}^{(2)} \quad \ldots \quad \boldsymbol{s}_{N-1,\Delta}^{(2)}\right]^T \in \mathbb{R}^{N \times N} \end{aligned} \tag{39}$$

such that we obtain

$$\boldsymbol{y}^i = \boldsymbol{S}_{\Delta,N}^{(1)} \cdot \boldsymbol{y} + X_0 \boldsymbol{S}_{\Delta,N}^{(2)} \cdot \boldsymbol{d} \tag{40}$$

There are several ways to compute the slopes in $\boldsymbol{d}$. In the case of cubic splines, they are defined through a set of linear equations which assumes that the second-order derivative of $y^i(x)$ is continuous

$$\left.\frac{d^2 y^i(x)}{dx^2}\right|_{x = nX_0-} = \left.\frac{d^2 y^i(x)}{dx^2}\right|_{x = nX_0+} \tag{41}$$

or

$$\begin{aligned} &\frac{-6\frac{y(n) - y(n-1)}{X_0} + 4d(n) + 2d(n-1)}{X_0} \\ &\qquad = \frac{6\frac{y(n+1) - y(n)}{X_0} - 2d(n+1) - 4d(n)}{X_0} \end{aligned} \tag{42}$$

and rearranging we get

$$\begin{aligned} &d(n-1) + 4d(n) + d(n+1) \\ &\qquad = 3\frac{y(n+1) - y(n-1)}{X_0}, \end{aligned} \tag{43}$$

for each $n = [1, \ldots, N-2]$, which is a set of $N - 2$ linear equations for N unknowns $d(n)$.

To have a full set of N equations we add two more equations from the end conditions called "not-a-knot" conditions [33]

$$d(0) + 2d(1) = \frac{-5y(0) + 4y(1) + y(2)}{2X_0} \tag{45}$$

$$\begin{aligned} &2d(N-2) + d(N-1) \\ &\quad = \frac{-y(N-3) - 4y(N-2) + 5y(N-1)}{2X_0} \end{aligned} \tag{46}$$

These equations can be rewritten in matrix form, as shown in equation (44), as shown at the top of this page, or shortly as

$$\boldsymbol{d} = \frac{3}{X_0} \boldsymbol{A}^{-1} \boldsymbol{B} \boldsymbol{y} \tag{47}$$

Inserting this result in (40) we finally obtain

$$\begin{aligned} \boldsymbol{y}^i &= \boldsymbol{S}_{\Delta,N}^{(1)} \cdot \boldsymbol{y} + X_0 \boldsymbol{S}_{\Delta,N}^{(2)} \cdot \frac{3}{X_0} \boldsymbol{A}^{-1} \boldsymbol{B} \boldsymbol{y} \\ &= \underbrace{\left(\boldsymbol{S}_{\Delta,N}^{(1)} + 3\boldsymbol{S}_{\Delta,N}^{(2)} \boldsymbol{A}^{-1} \boldsymbol{B}\right)}_{\boldsymbol{S}_{\Delta,N}} \boldsymbol{y} \end{aligned} \tag{48}$$

Thus, the matrix $\boldsymbol{S}_{\Delta,N}$ is fully determined by the conversion factor Δ and the number of samples N assuming that the common data point is $x = 0$. The matrix $\boldsymbol{S}_{\Delta,N}$ is used in (12b).

REFERENCES

[1] J. Zhang, I. Podkurkov, M. Haardt, and A. Nadeev, "Efficient multidimensional parameter estimation for joint wideband radar and communication systems based on OFDM," in *Proc. IEEE Int. Conf. Acoust., Speech, Signal Process. (ICASSP)*, New Orleans, LA, USA, Mar. 2017, pp. 3096–3100.

[2] C. Sturm and W. Wiesbeck, "Waveform design and signal processing aspects for fusion of wireless communications and radar sensing," *Proc. IEEE*, vol. 99, no. 7, pp. 1236–1259, Jul. 2011.

[3] M. Braun, "OFDM radar algorithms in mobile communication networks," Ph.D. dissertation, Commun. Eng. Lab, Karlsruhe Inst. Technol., Karlsruhe, Germany, 2014.

[4] C. Sturm, T. Zwick, and W. Wiesbeck, "An OFDM system concept for joint radar and communications operations," in *Proc. IEEE Int. Veh. Technol. Conf. (VTC)*, Apr. 2009, pp. 1–5.

[5] C. Sturm, M. Braun, T. Zwick, and W. Wiesbeck, "A multiple target Doppler estimation algorithm for OFDM based intelligent radar systems," in *Proc. Eur. Radar Conf. (EuRAD)*, Sep. 2010, pp. 73–76.

[6] A. D. Harper, J. T. Reed, J. L. Odom, and A. D. Lanterman, "Performance of a joint radar-communication system in doubly-selective channels," in *Proc. 49th Asilomar Conf. Signals, Syst. Comput.*, Nov. 2015, pp. 1369–1373.

[7] J. R. Krier, M. C. Norko, J. T. Reed, R. J. Baxley, A. D. Lanterman, X. Ma, and J. R. Barry, "Performance bounds for an OFDM-based joint radar and communications system," in *Proc. IEEE Military Commun. Conf. (MILCOM)*, Oct. 2015, pp. 511–516.

[8] J. Dickmann, N. Appenrodt, J. Klappstein, H.-L. Bloecher, M. Muntzinger, A. Sailer, M. Hahn , and C. Brenk, "Making bertha see even more: Radar contribution," *IEEE Access*, vol. 3, pp. 1233–1247, 2015.

[9] T. Wagner, R. Feger, and A. Stelzer, "Radar signal processing for jointly estimating tracks and micro-Doppler signatures," *IEEE Access*, vol. 5, pp. 1220–1238, 2017.

[10] P. Kumari, N. Gonzales-Prelcic, and R. W. Heath, Jr., "Investigating the IEEE 802.11ad standard for millimeter wave automotive radar," in *Proc. IEEE Int. Veh. Technol. Conf. (VTC)*, Apr. 2015, pp. 1–5.

[11] P. Papadimitratos, A. De La Fortelle, K. Evenssen, R. Brignolo, and S. Cosenza, "Vehicular communication systems: Enabling technologies, applications, and future outlook on intelligent transportation," *IEEE Commun. Mag.*, vol. 47, no. 11, pp. 84–95, Nov. 2009.

[12] E. Strom, H. Hartenstein, P. Santi, and W. Wiesbeck, "Vehicular communications: Ubiquitous networks for sustainable mobility," *Proc. IEEE*, vol. 98, no. 7, pp. 1111–1112, Jul. 2010.

[13] S. Dang, J. P. Coon, and G. Chen, "Outage performance of two-hop OFDM systems with spatially random decode-and-forward relays," *IEEE Access*, vol. 5, pp. 27514–27524, 2017.

[14] T. Do-Hong and P. Russer, "Signal processing for wideband smart antenna array applications," *IEEE Microw. Mag.*, vol. 5, no. 1, pp. 57–67, Mar. 2004. [Online]. Available: https://ieeexplore.ieee.org/author/38305847400

[15] F. Raimondi, P. Comon, and O. Michel, "Wideband multilinear array processing through tensor decomposition," in *Proc. IEEE Int. Conf. Acoust., Speech, Signal Process. (ICASSP)*, Shanghai, China, Mar. 2016, pp. 2951–2955.

[16] H. Krim and M. Viberg, "Two decades of array signal processing research: The parametric approach," *IEEE Signal Process. Mag.*, vol. 13, no. 4, pp. 67–94, Jul. 1996.

[17] B. D. Van Veen and K. M. Buckley, "Beamforming: A versatile approach to spatial filtering," *IEEE ASSP Mag.*, vol. 5, no. 2, pp. 4–24, Apr. 1988.

[18] H. Wang and M. Kaveh, "Coherent signal-subspace processing for the detection and estimation of angles of arrival of multiple wide-band sources," *IEEE Trans. Acoust., Speech, Signal Process.*, vol. ASSP-33, no. 4, pp. 823–831, Aug. 1985.

[19] B. Ottersten and T. Kailath, "Direction-of-arrival estimation for wide-band signals using the ESPRIT algorithm," *IEEE Trans. Acoust., Speech Signal Process.*, vol. 38, no. 2, pp. 317–327, Feb. 1990.

[20] H. Hung and M. Kaveh, "Coherent wide-band ESPRIT method for directions-of-arrival estimation of multiple wide-band sources," *IEEE Trans. Acoust., Speech Signal Process.*, vol. 38, no. 2, pp. 354–356, Feb. 1990.

[21] M. A. Doran, M. A. Doron, and A. J. Weiss, "Coherent wide-band processing for arbitrary array geometry," *IEEE Trans. Signal Process.*, vol. 41, no. 1, p. 414, Jan. 1993.

[22] S. Simanapalli and M. Kaveh, "Broadband focusing for partially adaptive beamforming," *IEEE Trans. Aerosp. Electron. Syst.*, vol. 30, no. 1, pp. 68–80, Jan. 1994.

[23] B. Friedlander and A. J. Weiss, "Direction finding for wide-band signals using an interpolated array," *IEEE Trans. Signal Process.*, vol. 41, no. 4, pp. 1618–1634, Apr. 1993.

[24] M.-Y. Cao, S. A. Vorobyov, and A. Hassanien, "Transmit array interpolation for DOA estimation via tensor decomposition in 2-D MIMO radar," *IEEE Trans. Signal Process.*, vol. 65, no. 19, pp. 5225–5239, Oct. 2017.

[25] H. Clergeot and O. Michel, "New simple implementation of the coherent signal subspace method for wide band direction of arrival estimation," in *Proc. Int. Conf. Acoust., Speech, Signal Process.*, vol. 4, May 1989, pp. 2764–2767.

[26] J. Krolik and D. Swingler, "Focused wide-band array processing by spatial resampling," *IEEE Trans. Acoust., Speech Signal Process.*, vol. 38, no. 2, pp. 356–360, Feb. 1990.

[27] Y.-H. Chen and R.-H. Chen, "Directions-of-arrival estimations of multiple coherent broadband signals," *IEEE Trans. Aerosp. Electron. Syst.*, vol. 29, no. 3, pp. 1035–1043, Jul. 1993.

[28] R. E. Crochiere and L. R. Rabiner, *Multirate Digital Signal Processing*. Englewood Cliffs, NJ, USA: Prentice-Hall, 1983.

[29] M. Haardt, F. Roemer, and G. Del Galdo, "Higher-order SVD-based subspace estimation to improve the parameter estimation accuracy in multidimensional harmonic retrieval problems," *IEEE Trans. Signal Process.*, vol. 56, no. 7, pp. 3198–3213, Jul. 2008.

[30] L. de Lathauwer, B. de Moor, and J. Vanderwalle, "A multilinear singular value decomposition," *SIAM J. Matrix Anal. Appl.*, vol. 21, no. 4, pp. 1253–1278, 2000.

[31] Y. L. Sit, C. Sturm, L. Reichardt, T. Zwick, and W. Wiesbeck, "The OFDM joint radar-communication system: An overview," in *Proc. Int. Conf. Adv. Satellite Space Commun.(SPACOMM)*, Apr. 2011, pp. 69–74.

[32] Y. L. Sit and T. Zwick, "MIMO OFDM radar with communication and interference cancellation features," in *Proc. IEEE Radar Conf*, May 2014, pp. 0265–0268.

[33] C. de Boor, *A Practical Guide to Splines*, vol. 27, 1st ed. New York, NY, USA: Springer-Verlag, 1978.

[34] C. E. Shannon, "Communication in the presence of noise," *Proc. IRE*, vol. 37, pp. 10–21, Feb. 1949.

[35] J. P. C. L. da Costa, F. Roemer, M. Haardt, and R. T. de Sousa, Jr., "Multidimensional model order selection," *EURASIP J. Adv. Signal Process.*, vol. 2011, p. 26, Jul. 2011.

[36] S. M. Kay, *Modern Spectral Estimation*. New York, NY, USA: Prentice-Hall, 1997.

[37] F. Roemer, M. Haardt, and G. D. Galdo, "Analytical performance assessment of multi-dimensional matrix- and tensor-based ESPRIT-type algorithms," *IEEE Trans. Signal Process.*, vol. 62, no. 10, pp. 2611–2625, May 2014.

[38] F. Roemer, E.-K. Kasnakli, Y. Cheng, and M. Haardt, "Tensor subspace tracking via Kronecker structured projections (TeTraKron)," in *Proc. IEEE 5th Int. Workshop Comput. Adv. Multi-Sensor Adapt. Process. (CAMSAP)*, Saint Martin, French, Dec. 2013, pp. 212–215.

[39] Y. Cheng, F. Roemer, O. Khatib, and M. Haardt, "Tensor subspace Tracking via Kronecker structured projections (TeTraKron) for time-varying multidimensional harmonic retrieval," *EURASIP J. Adv. Signal Process.*, vol. 2014, p. 123, Aug. 2014.

IVAN PODKURKOV (S'16) received the B.E. degree in telecommunications from Kazan National Research Technical University - KAI (KNRTU-KAI), Russia, in 2014, and the M.Sc. degree in communications and signal processing from the German Russian Institute of Advanced Technologies (GRIAT) organized between KNRTU-KAI, and the Ilmenau University of Technology (TUIL), Germany, as a double degree program, in 2016. He is currently pursuing on the Double Ph.D. program between KNRTU-KAI, former Kazan Aviation Institute, and TUIL.

From 2014 to 2016, he was an Engineer, and from 2016 to 2018, he was a Part-Time Teaching Assistant with the Department of Radio Electronic and Telecommunication Systems, Radio Electronic and Telecommunication Institute, KNRTU-KAI. Since 2016, he has been an Electrical Engineer with ELEPS Ltd. He is currently with the Department of Radio Electronic and Telecommunication Systems, KNRTU-KAI, and the Communications Research Laboratory (CRL), TUIL. His research interests include radar, direction of arrival estimation, statistical signal processing, communication-radar systems, multi-dimensional signal processing, and advanced non-Gaussian interference models.

JIANSHU ZHANG (S'09–M'15) received the B.E. degree in computer science from Sichuan University, China, the MBA degree in global management, the M.Sc. degree in electrical engineering from the Bremen University of Applied Sciences, the M.Sc. degree in computer science and communications engineering from the University of Duisburg-Essen, and the Dr.Ing. degree in electrical engineering from the Ilmenau University of Technology, Germany, in 2003, 2004, 2006, 2009, and 2014, respectively.

From 2010 to 2014, he was a Research Assistant with the Communications Research Laboratory, Ilmenau University of Technology, where he was a Post-Doctoral Researcher, from 2015 to 2017. Since 2018, he has been a Wireless Signal Processing Engineer with Intel Deutschland GmbH. His research interests include multi-dimensional signal processing, optimization theory, MIMO communications, and channel estimation.

ADEL FIRADOVICH NADEEV received the Diplom-Ingenieur (M.S.) degree and the Doktor-Ingenieur (Ph.D.) degree in radio electronic devices from the Kazan Aviation Institute, currently Kazan National Research Technical University - KAI (KNRTU-KAI), Russia, in 1987 and 1991, respectively. From 1987, he was an Engineer till 1992, then, as an Associate Professor, and since 2003, as a Full Professor, with the Department of Radio Electronic and Telecommunication Systems, KNRTU-KAI, where he has been a Full Professor with the Radio Electronic and Telecommunication Institute, since 2003. He was a Vice-Rector with KNRTU-KAI, from 2011 to 2012. He has been the Head of the Department of Radio Electronic and Telecommunication Systems and the Head of Radio Electronic and Telecommunication Institute, since 2012. His research interests include radio-electronic and communication systems, non-Gaussian interference probability models and methods, signal processing in the non-Gaussian channels, and the methods of modeling and optimization. He was the Technical Co-Chair of International Conference on Problems of Technique and Technology of Telecommunications (PTiTT), from 2008 to 2018, in Russia, and the SINKHROINFO 2017, under IEEE auspices, in Kazan, Russia.

MARTIN HAARDT (S'90–M'98–SM'99–F'18) received the Diplom-Ingenieur (M.S.) degree from Ruhr-University Bochum, Germany, in 1991, and the Doktor-Ingenieur (Ph.D.) degree from the Munich University of Technology, in 1996, after studying electrical engineering at the Ruhr-University Bochum and Purdue University, USA.

In 1997 he joined Siemens Mobile Networks in Munich, Germany, where he was responsible for strategic research for third generation mobile radio systems. From 1998 to 2001, he was the Director for International Projects and University Cooperation in the mobile infrastructure business of Siemens in Munich, where his work focused on mobile communications beyond the third generation. From 2012 to 2017, he was an Honorary Visiting Professor with the Department of Electronics, University of York, U.K. He has been a Full Professor with the Department of Electrical Engineering and Information Technology and the Head of the Communications Research Laboratory, Ilmenau University of Technology, Germany, since 2001. His research interests include wireless communications, array signal processing, high-resolution parameter estimation, and numerical linear and multi-linear algebra.

Dr. Haardt has been an elected member of the Sensor Array and Multichannel (SAM) technical committee of the IEEE Signal Processing Society, since 2011, where he currently serves as the Past Chair (Chair, from 2017 to 2018). He has received the 2009 Best Paper Award from the IEEE Signal Processing Society, the Vodafone (formerly Mannesmann Mobilfunk) Innovations-Award for outstanding research in mobile communications, the ITG best paper award from the Association of Electrical Engineering, Electronics, and Information Technology (VDE), and the Rohde & Schwarz Outstanding Dissertation Award. He has served as the Technical Co-Chair of PIMRC 2005 in Berlin, Germany, ISWCS 2010 in York, U.K., the European Wireless 2014 in Barcelona, and the Asilomar Conf. on Signals, Systems and Computers 2018 and as the General Co-Chair of ISWCS 2013 in Ilmenau, Germany, CAMSAP 2013 in Saint Martin, French Antilles, WSA 2015 in Ilmenau, SAM 2016 in Rio de Janeiro, Brazil, CAMSAP 2017 in Curacao, Dutch Antilles, and SAM 2020 in Hangzhou, China. He has served as a Senior Editor for the IEEE JOURNAL OF SELECTED TOPICS INCLUDE SIGNAL PROCESSING, since 2019, as an Associate Editor for the IEEE TRANSACTIONS ON SIGNAL PROCESSING, from 2002 to 2006 and from 2011 to 2015, the IEEE SIGNAL PROCESSING LETTERS, from 2006 to 2010, the *Research Letters in Signal Processing*, from 2007 to 2009, the Hindawi-*Journal of Electrical and Computer Engineering*, since 2009, and the *EURASIP Signal Processing Journal*, from 2011 to 2014, and as a Guest Editor for the *EURASIP Journal on Wireless Communications and Networking*.

• • •